Tectonic slicing of subducting oceanic crust along plate interfaces: Numerical modeling

Jonas Ruh, Laetitia Le Pourhiet, Philippe Agard, Evguenii Burov, T. Gerya

▶ **To cite this version:**

Jonas Ruh, Laetitia Le Pourhiet, Philippe Agard, Evguenii Burov, T. Gerya. Tectonic slicing of subducting oceanic crust along plate interfaces: Numerical modeling. Geochemistry, Geophysics, Geosystems, 2015, 16 (10), pp.3505-3531. 10.1002/2015GC005998 . hal-01207648

HAL Id: hal-01207648
https://hal.science/hal-01207648

Submitted on 24 Nov 2015

HAL is a multi-disciplinary open access archive for the deposit and dissemination of scientific research documents, whether they are published or not. The documents may come from teaching and research institutions in France or abroad, or from public or private research centers.

L'archive ouverte pluridisciplinaire **HAL**, est destinée au dépôt et à la diffusion de documents scientifiques de niveau recherche, publiés ou non, émanant des établissements d'enseignement et de recherche français ou étrangers, des laboratoires publics ou privés.

AGU PUBLICATIONS

Geochemistry, Geophysics, Geosystems

RESEARCH ARTICLE
10.1002/2015GC005998

Key Points:
- Effect of oceanic mantle serpentinization on crustal slicing
- Discontinuous mantle serpentinization leads to deep crustal slicing
- Metamorphic and structural results are compared to natural observations

Supporting Information:
- Supporting Information S1

Correspondence to:
J. Ruh,
jonas.ruh@upmc.fr

Citation:
Ruh, J. B., L. Le Pourhiet, P. Agard, E. Burov, and T. Gerya (2015), Tectonic slicing of subducting oceanic crust along plate interfaces: Numerical modeling, *Geochem. Geophys. Geosyst.*, *16*, doi:10.1002/2015GC005998.

Received 9 JUL 2015
Accepted 23 SEP 2015
Accepted article online 29 SEP 2015

© 2015. American Geophysical Union. All Rights Reserved.

Tectonic slicing of subducting oceanic crust along plate interfaces: Numerical modeling

J. B. Ruh[1,2], L. Le Pourhiet[1,2], Ph. Agard[1,2], E. Burov[1,2], and T. Gerya[3]

[1]Sorbonne Universites, UPMC Univ Paris 06, UMR 7193, Institut des Sciences de la Terre Paris (ISTeP), Paris, France, [2]CNRS, UMR 7193, Institut des Sciences de la Terre Paris (ISTeP), Paris, France, [3]Department of Earth Sciences, Institute of Geophysics, ETH, Zurich, Switzerland

Abstract Multikilometer-sized slivers of high-pressure low-temperature metamorphic oceanic crust and mantle are observed in many mountain belts. These blueschist and eclogite units were detached from the descending plate during subduction. Large-scale thermo-mechanical numerical models based on finite difference marker-in-cell staggered grid technique are implemented to investigate slicing processes that lead to the detachment of oceanic slivers and their exhumation before the onset of the continental collision phase. In particular, we investigate the role of the serpentinized subcrustal slab mantle in the mechanisms of shallow and deep crustal slicing. Results show that spatially homogeneous serpentinization of the sub-Moho slab mantle leads to complete accretion of oceanic crust within the accretionary wedge. Spatially discontinuous serpentinization of the slab mantle in form of unconnected patches can lead to shallow slicing of the oceanic crust below the accretionary wedge and to its deep slicing at mantle depths depending on the patch length, slab angle, convergence velocity and continental geothermal gradient. *P-T* paths obtained in this study are compared to natural examples of shallow slicing of the Crescent Terrane below Vancouver Island and deeply sliced crust of the Lago Superiore and Saas-Zermatt units in the Western Alps.

1. Introduction

Fragments of once subducted oceanic lithosphere (i.e., mafic/ultramafic blueschists and eclogites) line up in many orogenic sutures and still active subduction zones [*Agard et al*., 2009; *Guillot et al*., 2009; *Maruyama et al*., 1996]. Examples include >10 km long slivers of accreted and metamorphosed ophiolites exhumed during ongoing subduction (e.g., Raspas Complex, Ecuador: *Arculus et al*. [1999]; Crescent and Silesia Terranes, Cascadia: *Hyndman* [1995]) or toward the end of subduction (e.g., Western Alps: *Amato et al*. [1999]; *Angiboust et al*. [2009, 2012]; *Reinecke* [1998]). Unlike buoyant continental HP-LT rocks, which can be recovered from depths >100–300 km [*Chopin*, 1984; *Dobrzhinetskaya et al*., 1996], no oceanic rock slivers are returned from depths beyond ~80 km [*Agard et al*., 2009], as a result of rock densification [*Agard et al*., 2009] and/or increased mechanical coupling with the upper plate as a result of convection [*Syracuse et al*., 2010; *Wada and Wang*, 2009]. Age constraints indicate that the exhumation of these volumetrically subordinate fragments (generally as tectonic slices), made of high-pressure low-temperature (HP-LT) crustal material and up to ~1 km thick serpentinized mantle [*Angiboust and Agard*, 2010; *Li et al*., 2004], is short-lived and relatively rare in the lifetime of any given subduction zone [*Agard et al*., 2009].

Over the last three decades, emphasis was placed on understanding the mechanisms of exhumation [e.g., *Platt*, 1993] rather than how metamorphic rocks detach from the down-going plate (i.e., hereafter referred to as tectonic slicing; Figure 1). Whether the punctuated, episodic record of HP-LT events results from transient exhumation and/or transient slicing from the slab is completely unknown [*Monie and Agard*, 2009; *Plunder et al*., 2015]. Processes leading to the detachment of these oceanic slivers from the slab are nevertheless particularly crucial for the understanding of long- (and short-) term mechanical coupling along the plate interface.

A priori, three main factors/processes should control the detachment of an oceanic sliver from a descending plate: i) the degree of the mechanical coupling between the top of the slab and the overriding plate, which depends on the upper plate temperature and rheology, fluid pressure along the subduction interface, convergence velocity and amount of mantle wedge hydration [*Conrad et al*., 2004; *Heuret and Lallemand*, 2005;

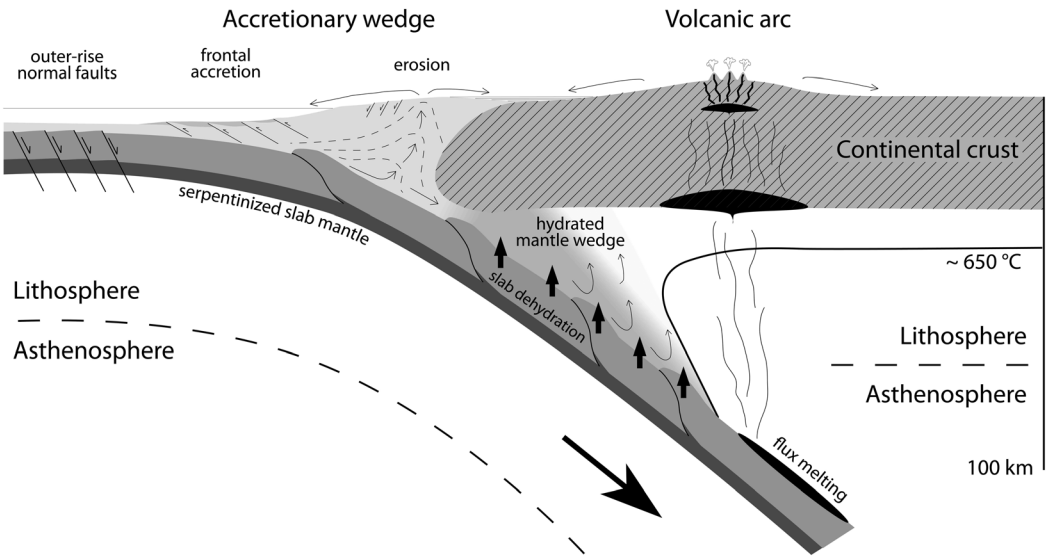

Figure 1. Schematic profile of an oceanic lithosphere subducting beneath a continental plate. Oceanic crust potentially detaches along serpentinized slab mantle. Exhumation occurs as corner flow within accretionary wedges or as channel flow in the hydrated mantle wedge.

et al., 1997], ii) the strength of the upper portion of the oceanic lithosphere (i.e., oceanic crust, in first approximation), which can be decreased by dehydration embrittlement [*Hacker et al*., 2003], hydration along fault planes prior to subduction [*Faccenda et al*., 2009; *Ranero et al*., 2003], crustal discontinuities [*Gorczyk et al*., 2007a] or localized melting [*Kanamori et al*., 1998], and iii) the ability to decouple the oceanic crust from the mantle lithosphere and therefore localize strain within the slab. Whatever the mechanism, the detachment of large slivers (>10 km) of oceanic lithosphere requires intermittent, probably switch-like, migration of the plate interface from the slab/mantle wedge boundary into the slab itself, which is mechanically analogous to what is observed in sedimentary wedges with several décollement levels [*Ruh et al*., 2012].

Serpentinites are likely to be a major player in all of the above mechanisms. Several studies have already suggested their role during exhumation, by lowering bulk viscosity and stresses needed [*Gerya et al*., 2002] to reach return forced flow of deeply subducted (and previously detached) material within a subduction channel [*Burov and Yamato*, 2008; *Cloos and Shreve*, 1988a, 1988b; *Guillot et al*., 2001, 2015; *Schmidt and Poli*, 1998; *Yamato et al*., 2007] and, by encasing rocks and lowering densities, in buoyancy-driven exhumation (as for the presence of less dense continental material [*Chemenda et al*., 1995]). Deep-slab dehydration along serpentinized faults is also thought to be the source of earthquakes in lower planes of double seismic zones [*Faccenda et al*., 2012; *Peacock*, 2001].

Of the above mentioned factors, only little work has been done on investigating the role of a serpentinized lithospheric slab mantle in decoupling the oceanic crust from the descending slab and detaching oceanic slivers in a physically consistent framework [*Vogt and Gerya*, 2014], thus justifying a numerical modelling study. *Vogt and Gerya* [2014] have shown that increased thickness and increased serpentine content below the oceanic crust enhance slicing but pointed out as well the importance of plate coupling during process. However, the role of slab mantle serpentinites appears to be very important because many observations such as ocean drilling suggest that seafloor peridotites can be extensively serpentinized (50–100%) [*Fruh-Green et al*., 1996] as a result of (i) sea water hydrothermal alteration [*Janecky and Seyfried*, 1986; *Martin and Fyfe*, 1970] along large-scale detachment faults [*McCaig et al*., 2007; *Tucholke et al*., 1998] and transform faults off-axis mid-ocean ridges [*Cann et al*., 1997; *Kelley et al*., 2001] or in increased fluid-flux areas at midplate regions [*Hutnak et al*., 2008], and (ii) infiltration of seawater into deep bending normal faults at the outer rise prior to subduction [*Ivandic et al*., 2010; *Ranero et al*., 2003]. Serpentinite patches are observed to be discontinuous within the oceanic lithosphere [*Cannat et al*., 1995] and wide-angle seismic experiments constrained serpentinite layer thicknesses of 2–3 km below the crust close to ridges [*Muller et al*., 1997], in line with maximum thicknesses observed in tectonic slices

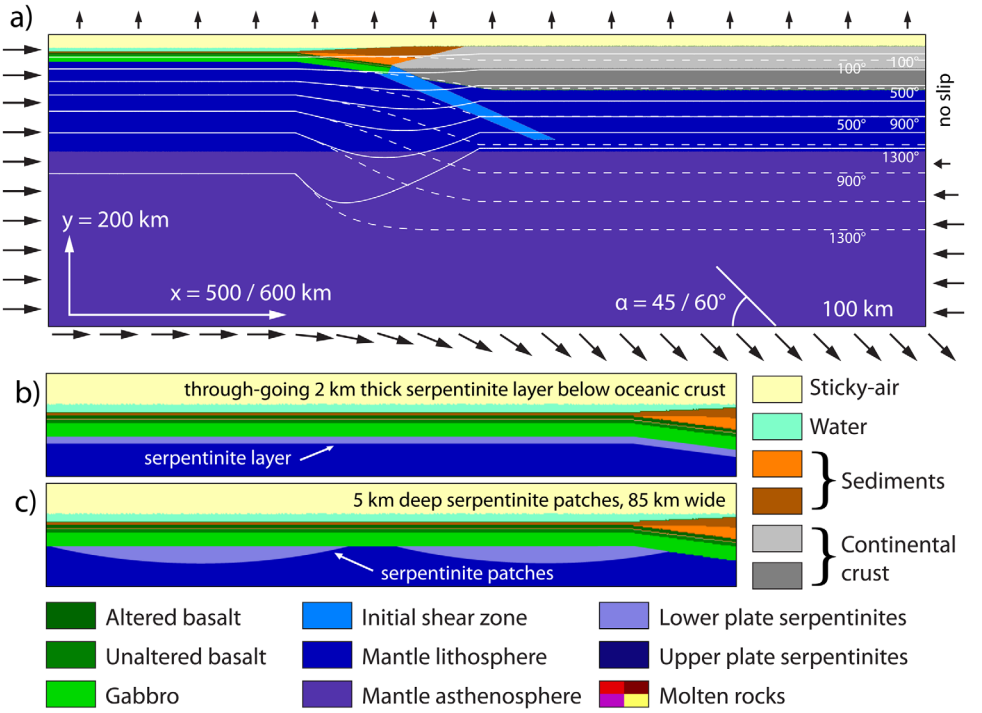

Figure 2. Model setup. (a) Complete model size. Colors define initial rock marker type. White lines illustrate initial temperature distribution (Full line: "warm" continent; Dashed line: "cold" continent). Arrows: lateral velocity boundary conditions, (b) initial distribution of continuous oceanic mantle serpentinization. (c) Initial distribution of discontinuous distribution with medium-sized patches (85 km).

of mountain belts [*Angiboust and Agard*, 2010; *Tartarotti et al*., 1986] and numerical models based on hydrothermal convection [*Iyer et al*., 2010].

We herein use large-strain thermo-mechanical numerical models to assess the role (and extent) of initial upper mantle serpentinization, upper plate geotherm, plate velocity, fluid pressure, and subduction angle on inter/intra-plate coupling. We then discuss the relevance of these models for natural examples of shallow (i.e., Crescent Terrane, Vancouver Island) and deep slicing (i.e., Monviso and Zermatt-Saas, Western Alps).

2. Model Setup

We use an optimized version of the implicit thermo-mechanical numerical code I2VIS [*Gerya and Yuen*, 2003] that implements direct solver PARDISO [*Schenk and Gartner*, 2004, 2006] to solve quasi-static equations for conservation of mass and momentum in an effectively viscoplastic incompressible medium. This code is based on the finite difference method with a fully staggered Eulerian grid and allows computing time evolution of the velocity, temperature and pressure fields. Large displacements are accounted through advection of Lagrangian markers (that bear material properties) according to the computed velocity field. Eulerian and Lagrangian grid spacing and governing equations including their numerical implementation are detailed in Appendix A.

2.1. Initial Geometry and Boundary Conditions

Boundary conditions and initial geometries of lithospheric and mantle rocks are set to obtain a stable steady state subduction of an oceanic plate below a continental one with a subduction angle α of either 45° or 60° (Figure 2a). The length of the models has been adjusted to the dip of the slab with 500 km ($\alpha = 60°$) and 600 km ($\alpha = 45°$) in *x* direction. Models are 200 km thick in *y* direction.

Thermal and mechanical material properties determining rock flow laws are obtained in laboratory experiments (Table 1) [*Ranalli*, 1995; *Hilairet et al*., 2007]. Properties depending on rock type are stored on Lagrangian markers and distributed as follows: the continental lithosphere consists of a 30 km thick felsic crust and of a mantle part, whose thickness depends on thermal distribution. The oceanic lithosphere has a

Table 1. Material Properties

	A_D (Pa^{-n}·s^{-1})	E (kJ/mol)	V (J/bar)	n (-)	φ (°)[a]	C (Pa)[a]	λ[b]	C_p (kJ·kg^{-1}·K^{-1})	k (W·m^{-1}·K^{-1})[c]	H_r (μW·m^3)
Sticky-air	10^{17}	0	0.8	1				3330	$200{\cdot}e^{(0.000004{\cdot}P)}$	0
Water	10^{17}	0	0.8	1				3.33	$200{\cdot}e^{(0.000004{\cdot}P)}$	0
Sediments[d]	1.97×10^{17}	154	0.8	2.3	30 (23.6)	10^7 (10^6)	0.95	1	$[0.64 + 807/(T+77)]{\cdot}e^{(0.000004{\cdot}P)}$	2
Continental crust[d]	1.97×10^{17}	154	0.8	2.3	30 (23.6)	10^7 (10^6)	0	1	$[0.64 + 807/(T+77)]{\cdot}e^{(0.000004{\cdot}P)}$	1
Basalt[d]	4.80×10^{22}	238	0.8	3.2	30 (23.6)	10^7 (10^6)	0.4, 0.98	1	$[1.18 + 474/(T+77)]{\cdot}e^{(0.000004{\cdot}P)}$	0.25
Gabbro[d]	4.80×10^{22}	238	0.8	3.2	30 (23.6)	10^7 (10^6)	0	1	$[1.18 + 474/(T+77)]{\cdot}e^{(0.000004{\cdot}P)}$	0.25
Mantle[d]	3.98×10^{16}	532	0.8	3.5	36.9 (23.6)	10^7 (10^6)	0	1	$[0.73 + 1293/(T+77)]{\cdot}e^{(0.000004{\cdot}P)}$	0.022
Initial shear zone[d]	5.01×10^{20}	470	0.8	4	5.7 (2.9)	10^7 (10^6)	0	1	$[0.73 + 1293/(T+77)]{\cdot}e^{(0.000004{\cdot}P)}$	0.022
Hydrated mantle[d]	5.01×10^{20}	470	0.8	4	36.9 (23.6)	10^7 (10^6)	0	1	$[0.73 + 1293/(T+77)]{\cdot}e^{(0.000004{\cdot}P)}$	0.022
Serpentinites[e]	3.21×10^{36}	8.9	0.32	3.8	17.5 (8.6)	10^7 (10^6)	0	1	$[0.73 + 1293/(T+77)]{\cdot}e^{(0.000004{\cdot}P)}$	0.022

[a]values in brackets denote friction angle and cohesion in weakened state depending on plastic strain, whit a linear decrease between strain $0 < \varepsilon < 1$.
[b]λ linearly decreases toward zero between 30 and 50 km depth.
[c]in MPa, T in K.
[d]*Ranalli* [1995].
[e]*Hilairet et al.* [2007].

commonly inferred structure [e.g., *Schubert et al.*, 1976] and consists, from top to bottom, of a 1 km thick sediment layer, 1 km of hydrothermally altered (mechanically weakened) basalt, 1 km of unaltered basalt, a 4 km thick gabbroic layer, and mantle lithosphere (whose thickness again depends on thermal distribution). The ocean floor is topped by a 2.5 km thick water column. The continent-ocean transition is defined by a zone of continental crust that progressively thins seaward, a downward-bended oceanic crust and a sediment-filled passive margin (Figure 2a). The upper interfaces of the ocean and continental crust are covered by respectively 9 km and 8 km thick low-density, low-viscosity "sticky-air" layer to implement an internal free surface [*Crameri et al.*, 2012]. Both lithospheric and asthenospheric mantle consist of anhydrous peridotite (Table 1). To initialize subduction, we prescribe a rheologically weak initial shear zone that cuts the entire lithosphere (Figure 2a). The importance of such preexisting weakness zones for the initiation of subduction has been commonly inferred in previous studies [e.g., *Cloetingh et al.*, 1982; *Gurnis*, 1992; *Nikolaeva et al.*, 2010].

Constant velocities are applied along all lateral boundaries (Figure 2a). From the left side, material enters the Eulerian box with a rate v_x. Through the bottom boundary, material leaves the box with v_x according to a velocity field direction depending on the subduction angle α. The right-lateral boundary is prescribed as a no-slip boundary condition down to the lithosphere/asthenosphere transition and incoming material flux below. The velocity along the lower right boundary is set to ensure that the same area is coming into the Eulerian box as the area that leaves along the rightmost 100 km of the bottom boundary. This allows prescribing the location of the subduction interface at the lower boundary and introduces a stable mantle wedge flow in the lower right corner of the model. The top boundary is defined by a vertical velocity v_y that accounts for the incoming water and "sticky-air" material from the left boundary (11.5 km) and free-slip horizontally. Convergence velocities v_x are either 4 cm/yr (referred to as "slow" in text and figures) or 12 cm/yr (referred to as "fast").

The initial temperature distribution in the oceanic lithosphere is defined by an oceanic geotherm with a cooling age of 30 Myr [*Turcotte and Schubert*, 2002]. For the continental lithosphere, two initial thermal structures have been tested: (i) A "warm" continent with a thermal gradient of 18.6°C/km down to 72 km depth, and (ii) a "cold" continent exhibiting a thermal gradient of 10.4°C/km down to 132 km depth (Figure 2a). The background geothermal gradient below these depths is 0.5°C/km. Thermal boundary conditions are 0°C along the upper boundary, zero flux on both lateral sides and an open boundary at the bottom [*Gorczyk et al.*, 2007b].

2.2. Serpentinization of Oceanic Mantle Lithosphere

Serpentinization of oceanic mantle rocks results from hydrothermal alteration of mantle peridotite by sea water [*Janecky and Seyfried*, 1986; *Martin and Fyfe*, 1970], from their production at spreading centres to their descent into the mantle at subduction zones [*Fryer*, 2002]. Serpentinized, and therefore mechanically weakened [*Escartin et al.*, 1997; *Hilairet et al.*, 2007] sub-Moho lithospheric mantle could help decouple oceanic crust from the slab, thus leading to detachment of oceanic slivers. To test the influence of serpentinization

degree of oceanic mantle, different additional serpentinite units have been introduced below the oceanic crust in the upper mantle (Figure 2a). A first series of numerical experiments test the hypothesis of an initially continuous, 2 km thick serpentinite layer below the oceanic crust (Figure 2b), following seismic [*Muller et al*., 1997] and deep-sea drilling observations [*Fruh-Green et al*., 1996], which will promote full mechanical decoupling between the oceanic crust and lithospheric mantle.

In further series of experiments, the continuous serpentinite layer is replaced by 5 km thick variably wide (42.5, 85, 127.5 km; Figure 2c) discontinuous serpentinite patches that provide partial mechanical decoupling between the oceanic crust and lithospheric mantle. Such discontinuous serpentinite patches have been observed within the oceanic lithosphere [*Cannat et al*., 1995]. Patchy serpentinization can be the result of multiple hydrothermal convection cells continuously generated along a mid-ocean ridge [*Iyer et al*., 2010]. Serpentinite patches are continuously introduced on the left side of the model, from which the new material arrives with velocity v_x. The intervals between serpentinite patches are 17.5, 15 and 12.5 km for models with small, medium and large patches, respectively.

2.3. Hydration, Density, and Melting Processes

Modeled rock facies can absorb and release free water depending on the equilibrium water content. This content is obtained for each lithology (except the continental crust, where it is constantly 1%) by free energy minimization [*Connolly*, 2005] as a function of pressure and temperature from thermodynamic data and rock compositions [*Gerya et al*., 2006]. Maximal water content values are 7.6 wt% for sediments, 2.78 wt% for upper and 1.47 wt% for lower oceanic crust, and 1.98 wt% for hydrated mantle [*Gerya et al*., 2006]. Additionally, 1 wt% of water is present as pore fluid in sediments and upper oceanic crust. It is expelled during burial in a manner that weight percentage of pore fluid decreases linearly to zero at 50 km depth. This release of water also reflects the dehydration of minerals at low temperatures [e.g., *Ranero et al*., 2008] that are not included in the thermodynamic database such as the smectite to illite transition at 60–160°C [*Perry and Hower*, 1970] and further transformations to muscovite at 250–300°C [*Frey*, 1987]. Deep dehydration of serpentinites (antigorite) to hydrated peridotite follows the stability field from *Schmidt and Poll* [1998].

In the numerical model, dehydration of rocks (according to the thermodynamic database) results in release of free water that is stored on newly formed water markers that migrate through the grid until they meet a rock that is not fully hydrated and able to absorb water. The velocity of water markers depends on local pressure gradients and the background mechanical velocity field:

$$v_{water} = v_i + \zeta \cdot k_i \tag{1}$$

where v_i denotes the viscous velocity field in x and y direction, ζ the percolation velocity (1 cm/yr in all numerical experiments) and k_i a pressure-dependent coefficient ($k_1 = k_x$, $k_2 = k_y$):

$$k_i = \frac{\rho_m g_i - \frac{\partial P}{\partial x_i}}{(\rho_m - \rho_f) g_2}, \quad |k_i|! \leq 2 \tag{2}$$

with p_m denoting a reference mantle density (3300 kg/m^3) and p_y fluid density (1000 kg/m^3). Upward movement is defined by positive values.

Densities of modeled rocks are computed from the equilibrium mineralogical composition computed for each lithology using the free energy minimization for given *P-T* conditions [*Connolly and Petrini*, 2002; *Gerya et al*., 2006; *Gorczyk et al*., 2007b]. Melting is taken into account as soon as local temperature exceeds a rock-specific solidus [see *Gerya and Meilick*, 2011, Table 1]. The volumetric degree of melting increases linearly from 0 (at solidus temperature) to 1 (at liquidus temperature). The melt amount extracted from partially molten rocks is stored on markers that migrate through the model domain in the same manner as fluids (equations (1) and (2)). For further information on the applied melting and melt extraction model see *Gerya and Meilick* [2011].

Fluids weaken rocks depending on the fluid pressure ratio λ ($= P_{fluid}/P_{litho}$), which lowers the calculated plastic yield strength (equation (A11)). In experiments presented here, a λ of 0.95 for sediments, which is in agreement with recent fluid pressure estimations [*Gosh et al*., 2010; *Gressier et al*., 2010; *Moore and Tobin*, 1997], and λ of 0.98 for altered basalts (<50 km depth) [*Moreno et al*., 2014] is applied that diminish linearly toward zero between 30 and 50 km depth (Table 1). This effect is implemented according to the loss of

Table 2. Numerical Experiments

Model	Oceanic Plate Serpentinization	Thermal Structure of Continental Plate	Convergence Velocity (cm/a)	Slab Angle (°)	Slicing of Oceanic Crust	Figure
noC45s	no	cold	4	45	no	3,7,11,S1
noW45s	no	warm	4	45	no	3,7,11,S1
conC45s	continuous	cold	4	45	shallow	4
conW45s	continuous	warm	4	45	shallow	4
midC45s	85 km patches	cold	4	45	deep	5,6,9,12
midW45s	85 km patches	warm	4	45	no	5,9
smC45s	42.5 km patches	cold	4	45	no	7,11,S2
smW45s	42.5 km patches	warm	4	45	no	7,11,S2
larC45s	170 km patches	cold	4	45	shallow/deep	8,13
larW45s	170 km patches	warm	4	45	shallow/deep	8
midC45f	85 km patches	cold	12	45	no	9,11
midW45f	85 km patches	warm	12	45	no	9,11
midC60s	85 km patches	cold	4	60	deep	10,13
midW60s	85 km patches	warm	4	60	deep	10,13
midC60f	85 km patches	cold	12	60	deep	10,13
midW60f	85 km patches	warm	12	60	deep	10,13

pore water with depth described above, and fluid flow and pore pressure estimations along subduction zone forearcs [*Saffer and Tobin*, 2011]. The effect of a varying λ with depth has been tested by conducting experiments with a static λ of 0.45, 0.7, and 0.98 along the subduction interface, i.e., within the hydrothermally altered upper oceanic crust (supporting information Figures S1–S3).

Furthermore, If free fluid markers (water or melt) are present, an increased λ can be introduced to weaken the rocks plastic strength. Here this effect is only taken into account for the lower oceanic crust ($\lambda = 1$), where phase transitions can lead to strong fluid over-pressures [e.g., *Austrheim and Boundy*, 1994].

2.4. Tracing the Active Subduction Interface

To better understand interplate coupling at subduction zones, it is important to investigate mechanical, thermal and chemical rock properties along the active plate interface. In a subduction zone, the main interface is located where the shear strain-rates are largest over a specific distance. In numerical models presented here, the subduction interface is tracked depending on the second invariant of the strain-rate tensor: all Lagrangian markers with a second invariant of the strain-rate tensor larger than a critical value are identified as part of the active subduction interface. The critical strain rate for "slow" experiments (v_x = 4 cm/yr) is $\dot{\varepsilon}_{cs} = 10^{-13}$ s^{-1}. For "fast" experiments (v_x = 12 cm/yr) it is $\dot{\varepsilon}_{cs} = 3{\cdot}10^{-13}$ s^{-1}. To reveal the evolution of these properties along the slab interface, we bin the identified markers according to their *y* coordinate with bins of 2 km for temperature and stress and 5 km for chemical composition, respectively. This allows representing the temperature, the second invariant of stress and relative percentage (Γ_i) of each lithology *i* as a function of depth. Γ_i is the ratio of markers of type *i* relative to total number of marker present in each bin.

3. Results

We test the influence of upper oceanic mantle serpentinization and inter-plate coupling on the mechanical, thermal and structural evolution of subduction zones. All model setups are tested with a "cold" and a "warm" overriding continental plate to investigate the effect of upper plate thermal gradient on coupling mechanisms. Numerical experiments without serpentinization of oceanic mantle material are presented first, then those with continuous and discontinuous layers of serpentinized mantle below the oceanic crust. Models with discontinuous serpentinization were applied to test the effects of i) convergence velocity, ii) slab angle, and iii) extent of serpentinite patches (Table 2).

3.1. No Oceanic Mantle Serpentinization

Numerical experiments without serpentinization of upper oceanic mantle are presented after 10 Myr (Figure 3), for "cold" and "warm" continental geotherms. For both models, sedimentary wedges grow by frontal accretion and important underplating at depths $<$35 km (Figure 3). At the bottom of the wedge, altered upper oceanic crust is strongly deforming and gets partly incorporated by underplating and comer flow. Fluids derived from

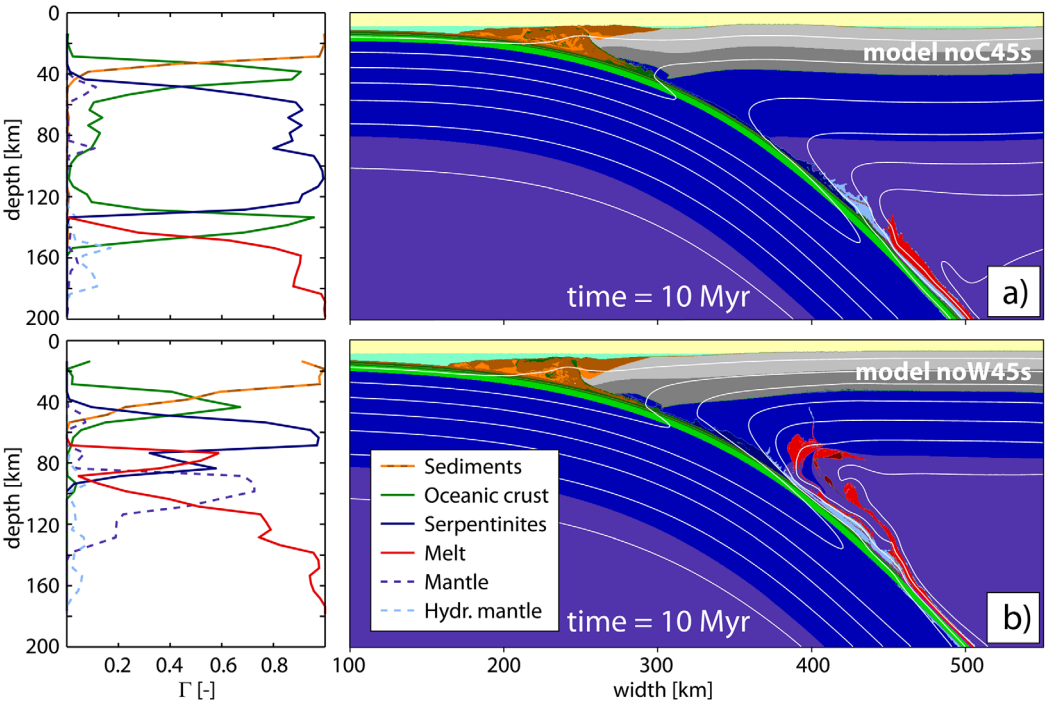

Figure 3. Experiments without slab serpentinization after ~10 Myr for (a) "cold" and (b) "warm" continental geotherms. (Left column) Percentages of rock type involved in the main subduction shear zone versus depth (markers with strain rates larger than 10^{-13} s^{-1}).

pores and dehydration of minerals at low temperature (see section 3.3) hydrate mantle peridotites of the overriding plate to form a thin layer (1–2 km) of serpentinite along the subduction interface below the accretionary wedge (Figure 3). Further down, deep dehydration of basalt and gabbros increases the fluid input into the continental mantle and widens the area of mantle serpentinization (~6 km thick layer). Antigorite destabilizes when temperatures reach 650–700°C [*Schmidt and Poli*, 1998] causing serpentinites to dehydrate and to become hydrated peridotite (Table 1).

Since the dehydration of oceanic crust and serpentinites depends on temperature and pressure, the geothermal gradient of the continental lithosphere strongly influences depths of crustal dehydration and continental mantle hydration. In the "cold" continent model (model noC45s), intense serpentinization of the mantle wedge begins ~80 km below the surface down to ~120km, where hydrated serpentinite-free mantle occurs (Figure 3a). Flux melting of mantle material and melting of upper oceanic crust occurs at depths >140 km. For a "warm" continent (model noW45s), dehydration of oceanic crust and according mantle serpentinization initiates at depths ~40 km below the surface. Dehydration of mantle wedge serpentinites occurs below ~80 km (Figure 3b).

In both "cold" and "warm" models the major shear zone is exclusively within sedimentary rocks at wedge levels (Figure 3, left column). The involvement of strongly deforming upper oceanic crustal rocks at depths of ~40 km below the surface indicates a step-down in subprism décollement and results in underplating and stacking of wedge material. Further down, the main displacement along the subduction interface occurs within serpentinites resulting from crustal dehydration (Figure 3, left column). In model noC45s, the subduction interface is localized along serpentinites from 40 to 120 km depths below the surface. In the upper 40 km, deformation also occurs within upper crust due to the very small thickness of the serpentinite layer (Figure 3a). Dehydration of serpentinites and subsequent strengthening of the mantle forces the shear zone into the upper crust again at ~140 km depth below surface (Figure 3a). Beyond these depths, areas of mantle melting provide least resistance to shearing. Model noW45s mainly shears along the serpentinized mantle from ~40 to 80 km below the surface (Figure 3b). The strong shearing along mantle material and deeper involvement of melts indicates that the subduction interface lies within mantle along the melt plume, dragging a piece of mantle material downward (Figure 3 and supporting information Figure S4). In general, the type of rock forming the major subduction shear zone has a strong influence on the coupling along the plate boundary.

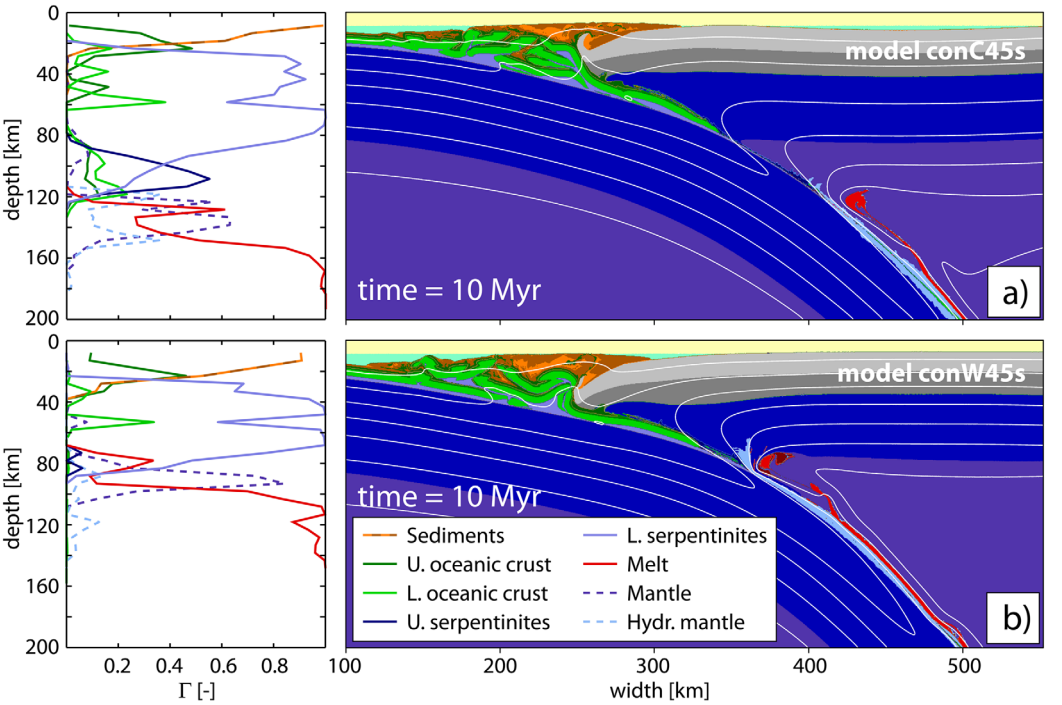

Figure 4. Experiments with continuous slab serpentinization after ~10 Myr for (a) "cold" and (b) "warm" continental geotherms. (Left column) Percentages of rock type involved in the main subduction shear zone versus depth (markers with strain rates larger than 10^{-13} s^{-1}).

The second invariant of the strain-rate tensor after 10 Myr is presented to better illustrate differences between "cold" and "warm" experiments (supporting information Figure S4). Both "cold" and "warm" models show plastic/brittle extensional faults along the outer-rise reaching as deep as 25–30 km into the oceanic plate, but this is larger in the colder experiments (supporting information Figure S4a). Listric normal faults form for both models in the sedimentary wedge and root in the basal décollement. The conspicuous shear zone at the base of the sedimentary wedge steps down into the upper crust where it splits up to form a splay fault. Further down, the two faults merge into one shear zone again (supporting information Figure S4). In model noC45s, the subduction shear zone is narrow and localized through the whole model. Temperature-dependent rheological behavior of the continental plate indicates a lithosphere thickness of 120–130 km (supporting information Figure S4a). Model noW45s exhibits more melting within the continental plate (Figure 3b) and introduces a weak rheology. High strain rates in the molten mantle indicate that the main subduction interface shifts into the upper plate mantle, leading to subduction of continental mantle pieces attached to the descending slab (supporting information Figure S4b). Rheological thickness of a "warm" continental lithosphere is between 70 and 80 km.

3.2. Continuous Oceanic Mantle Serpentization

After 10 Myr, the numerical experiments with a 2 km thick continuous layer of serpentinization below the oceanic crust differ strongly from models without serpentinites (Figure 4). All incoming oceanic crust, basalt and gabbro, is scratched off along the serpentinite layer in both "cold" and "warm" models (models conC45s and conW45s; Table 2). It can be accreted at the trench (Figure 4a) or underplated below the wedge, which leads to elevated temperatures at wedge levels (Figure 4; i.e., 300°C isotherm). Almost no oceanic crust and sediments are brought down to mantle levels where they would dehydrate extensively. Serpentinization of the overriding plate mantle is therefore very minor and predominantly occurring due to release of pore-water and low-temperature dehydration reactions (Figure 4). Nevertheless, much chemically bound water is brought into the mantle by subcrustal serpentinite within the subducting oceanic plate. Serpentinite dehydration (650–700°C) occurs respectively at ~120 km and ~80 km depths below surface for the "cold" and the "warm" simulation (Figure 4). Degree of mantle melting in models with a continuous layer of serpentinite is less than in models without serpentinisation (noC45s and noW45s) due to the decreased input of fluids.

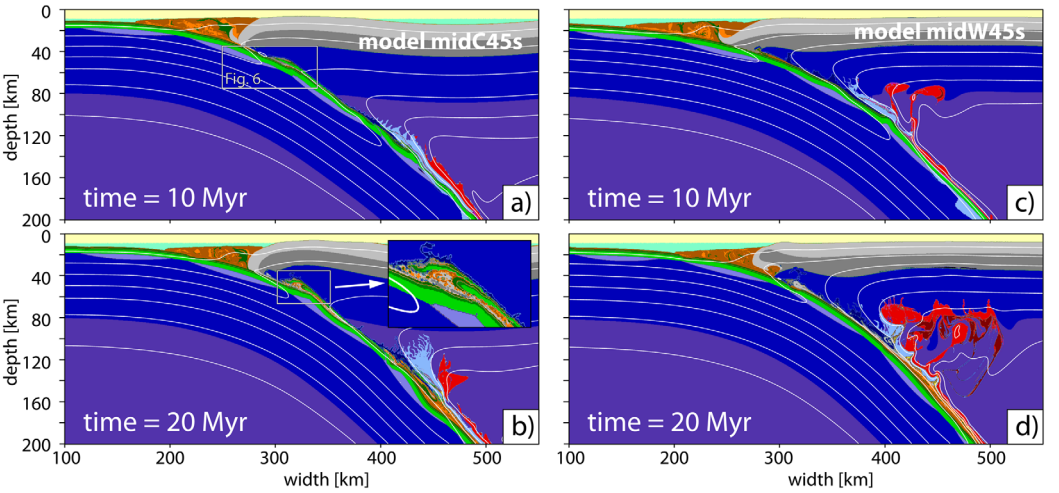

Figure 5. Snapshots of the reference model for experiments with discontinuous slab serpentinization after ~10 Myr and ~20 Myr for (a, b) "cold" and (c, d) "warm" continental geotherms.

In the uppermost 10–15 km below surface deformation occurs within sediments and upper oceanic crust (Figure 4, left column). Then, the active subduction interface is localized mainly within the oceanic serpentinite layer. This down-step of the shear zone is responsible for the peeling of the oceanic crust off the down-going plate. For both "cold" and "warm" experiment failure of the lower gabbroic oceanic crust is observed (Figure 4, left column). Failure of gabbroic rocks indicates thrusting of the oceanic crust. In both models, a peak deformation within gabbros occurs at depths around 50 km below the surface. These peaks are related to a thinning of the lower serpentinite layer. Temperature locally increases due to viscous shear heating (see isotherms; Figure 4). Model conC45s exhibits a subduction shear zone being active within a mash of gabbros and lower and upper plate serpentinites between 80 and 120 km below surface (Figure 4a). Below 120 km, the plate interface is located first along the boundary between molten and solid mantle rocks and deeper than 160 km along molten mantle. In model conW45s, upper plate serpentinites do not play any role as the interface is located within lower plate serpentinites until they are dehydrated above ~700°C at ~80 km below surface (Figure 4b). High strain rates in mantle rocks below and deeper localization within molten mantle indicates that pieces of upper plate mantle are brought downward with the slab as observed in "warm" experiment without oceanic plate serpentinization (model noW45s; Figure 3b).

One consequence of accreting almost the complete oceanic crust at wedge levels is that temperatures within the subducting slabs are much warmer (Figure 4) compared to experiments in which the cold oceanic crust enters the subduction zone (Figure 3). Furthermore, thrusting of oceanic crust and related thickening of the accretionary wedge due to crustal underplating increases the gravitational loading on the incoming lithosphere. After initial bending along the outer-rise, the slab descends at a more or less constant angle of 15–20° down to 100 km depth, where it bends to 40–45° (Figure 4).

3.3. Discontinuous Oceanic Mantle Serpentinization

In the experiments described above, the oceanic crust is either always coupled to the mantle below (models without oceanic plate serpentinization) or completely decoupled from the mantle (models with continuous serpentinite layer below the crust). In addition to these two end-member cases, a series of models with discontinuous serpentinization (Figure 2c) of the oceanic plate mantle was conducted. Reference numerical experiments for discontinuous oceanic mantle serpentinization are characterized by 85 km wide patches of serpentinite below the subducting oceanic crust, a subduction angle of 45°, and a convergence velocity of 4 cm/yr (models midC45s and midW45s; Table 2).

The numerical experiments are presented after 10 and 20 Myr time for "cold" (model midC45s) and "warm" (model midW45s) continental lithosphere (Figure 5). Oceanic crust is underthrusting the sedimentary wedge and passing the Moho depth levels without significant deformation, independent of the continental geothermal gradient. Only some altered basaltic rocks are scraped off the descending plate and incorporated into the accretionary wedge (Figure 5). At mantle depths, deformation within the slab and along the

subduction interface exhibits some major differences. In model midC45s, slices of oceanic crust (gabbro and basalt) are detached from the downgoing plate at ~45 km depth (Figure 5a). After 10 Myr, the detached sliver is interlaced with continental crust and minor sedimentary material. A thin ~1 km wide horizon of upper plate mantle serpentinite tops oceanic and continental crustal mélange from the continental Moho down to ~80 km depth below surface, where it widens due to deep oceanic crust dehydration. At ~50 km depth oceanic crust still attached to the downgoing slab deforms at the pinch-out of the lower plate serpentinite patch (Figure 5a). This compressional deformation and potential slicing of oceanic crust at the left pinch-out goes hand in hand with crustal boudinage along the right pinch-out of serpentinite patches (left and right denoting the position of serpentinite pinch-out when entering the trench). After 20 Myr the oceanic sliver detached but is still at sub-Moho depth levels, now accompanied by a second slice (Figure 5b).

Experiment midW45s lacks detachment of oceanic slivers from the downgoing plate. Although strong compressional deformation of oceanic crust occurs ~100 km below surface (Figure 5c), no coherent sliver is prevented to be subducted with the descending plate (Figure 5d). This crustal deformation appears to develop at depths when upper plate serpentinites dehydrate and rheology of the upper plate gets stronger. Similar to models without oceanic plate serpentinization (Figure 3), upper plate mantle serpentinization in "warm" experiments is increased at shallower levels in contrast to "cold" experiments due to shallower dehydration of oceanic crust. Furthermore, melting of mantle material is more extensive below "warm" continents (Figures 5c and 5d).

In both "cold" and "warm" experiments continental crust is sporadically eroded at the base from the overriding plate and brought down into the subduction channel. This is the case when continental crust interacts directly with the oceanic crust and the subduction shear zone is formed along the contact (Figures 5b and 5c). This "destructive" subduction alternates with a mode, where sediments are dragged into the subduction channel. In this case, the subduction interface lies between the sediments and the upper oceanic crust (Figures 5a and 5d). Large portions of sediments ($y > 120$ km) have been brought into the subduction channel. This also explains the smaller areas of sedimentary accretionary wedges after 20 Myr (Figures 5b and 5d). The mode flip between continental crust erosion and sediment subduction seems to be related to the subduction of sediment-filled graben structures that form due to outer-rise faulting at the trench (Figure 5d).

The dynamics of the detachment of a single oceanic crust sliver (models midC45s) is illustrated by marker distribution and strain-rate plots ranging over a period of 3 Myr (Figure 6). At 6.05 Ma, marker distribution indicates continental erosion as the current mode of subduction (Figure 6a). Although the main shear zone is still located above the oceanic crust (Figure 6f), the lower serpentinite patch already exhibits large strain rates (Figure 6a, left column). At 6.77 Ma, deformation is shifted toward the left pinch-out of the serpentinite patch and a shear band develops within the oceanic crust (Figures 6b and 6g). Within the upper 15 km the plate interface is mainly located within continental crust and upper plate serpentinites (top oceanic crust). From 50 to 75 km depth, a large part of the shear deformation occurs within lower serpentinites (Figure 6b, left column). At 7.61 Ma, the main shear zone slices the oceanic crust (Figures 6c and 6h). Distribution of markers with high strain rates clearly shows a down step of the subduction interface and shearing of oceanic crust (Figure 6c, left column). After thrusting and slicing a piece of oceanic crust (8.27 Ma), it remains at its position as the main shear zone passes below (Figures 6d and 6i). At 60–65 km depth, boudinage of the lower part of the sliver occurs and the shear zone is located along upper plate serpentinites (Figure 6d, left column). At 9.07 Ma, the subduction shear zone lays between the detached sliver and nondeforming subducting oceanic crust (Figures 6e and 6j). Nevertheless, high strain rates are observed within a newly subducted serpentinite patch (Figure 6e, left column), similar to earlier stages (Figures 6a and 6b).

3.3.1. Effect of Serpentinite Patch Size

The influence of serpentinization patch size on slicing of oceanic crust was tested by conducting identical experiments as discontinuous reference models (section 3.3.1) but with different oceanic mantle serpentinization wavelengths (42.5, 127.5 km), i.e., smaller and larger patches (Table 2). The experiments with smaller patches of serpentinized mantle below the oceanic crust (models smC45s and smW45s) do not exhibit slicing and detachment of coherent slivers of oceanic crust onto the overriding plate, independent of the thermal gradient of the continental plate (supporting information Figure S5). Model smC45s indicates zones of localized crustal deformation at the left tips of the subducted serpentinite patches (Figure 8a). An increase of crustal drag can be observed at depths >120 km, where upper plate serpentinites dehydrate. In model

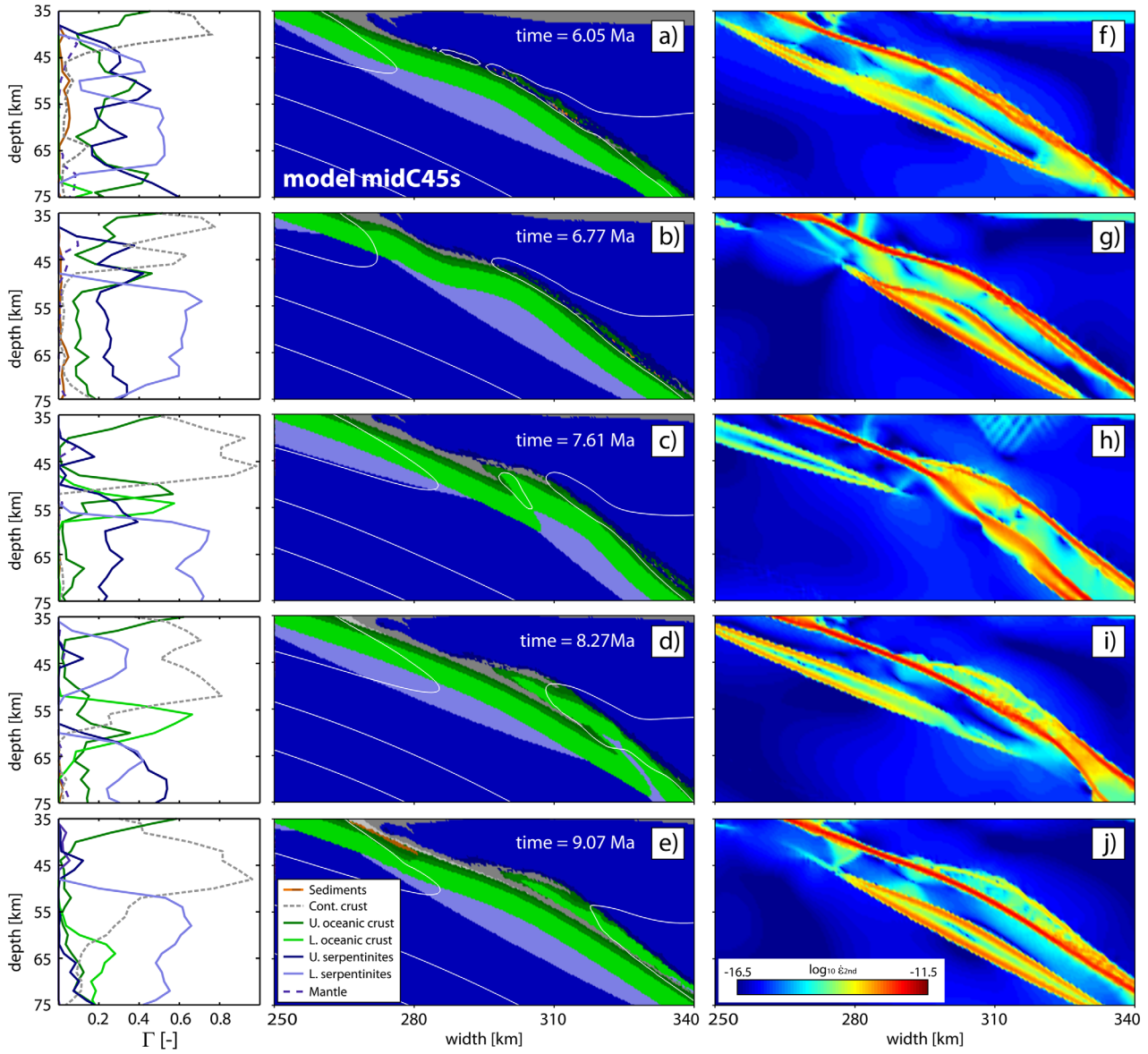

Figure 6. (a–e) Snapshots of marker distribution of the discontinuous reference model between 6 and 9 Myr. (f–j) According plots of the second invariant of the strain rate tensor. Left column: Percentages of rock type involved in the main subduction shear zone versus depth (markers with strain rates larger than 10^{-13} s^{-1}).

smW45s, deformation within the crust is observed from 80 to 100 km depths, due to shallower destabilization of serpentinites in the upper plate (Figure 8b).

Although oceanic crust seems to be much more deformed during subduction for numerical experiments with small patches (supporting information Figure S5), shear stresses within the lower crust are similar to those in models without oceanic serpentinization (Figure 7). The increase in shear stresses at deeper levels for "cold" continents is not affected by the presence or the size of the serpentines patches (Figure 7, black lines). Stresses within the crust mainly depend on the strength of the overriding plate and the resistance to shear along the plate interface. For experiment smC45s, shear stresses between 40 and 80 km depths are increased by a factor of ~2 in contrast to model smW45s (Figure 7b). This increase is not observed in experiments without serpentinite patches (Figure 7a).

In case of larger serpentinite patches (127.5 km), slicing of oceanic crust occurs independent of the continental geotherm (Figure 8). Differences between "cold" and "warm" experiments are similar as above: i) depth of dehydration of upper plate serpentinites that, to a large extend, form the subduction shear zone,

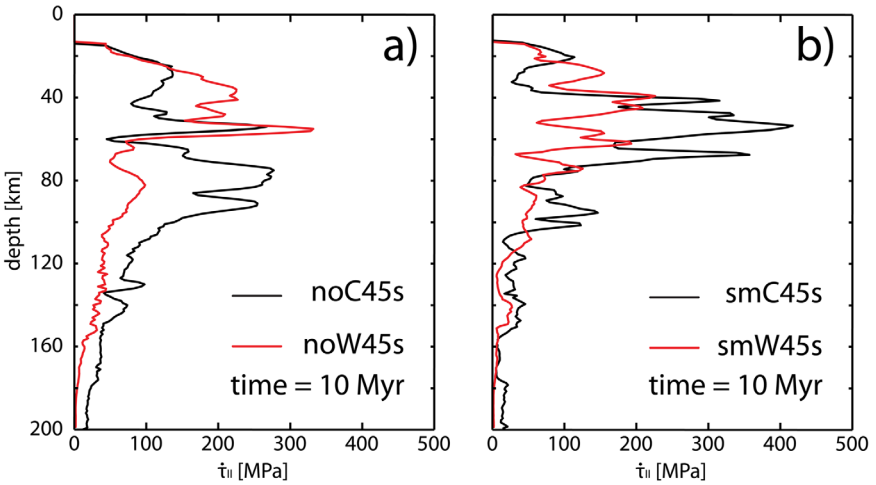

Figure 7. Averaged values of the second invariant of the stress tensor within lower oceanic crust (gabbro) of experiments without slicing: (a) "cold" (black) and "warm" (red) models without oceanic mantle serpentinization. (b) "Cold" (black) and "warm" (red) models with small patches of discontinuous oceanic mantle serpentinization (42.5 km).

and ii) amount of melt production due to fluid induced melting of the upper plate mantle. Time evolution models larC45s (Figures 8a–8d) and larW45s (Figures 8e–8h) illustrate that a similar mode of slicing of oceanic crust takes place. After ~6 Myr model time, thrusting and underplating of oceanic crust beneath the

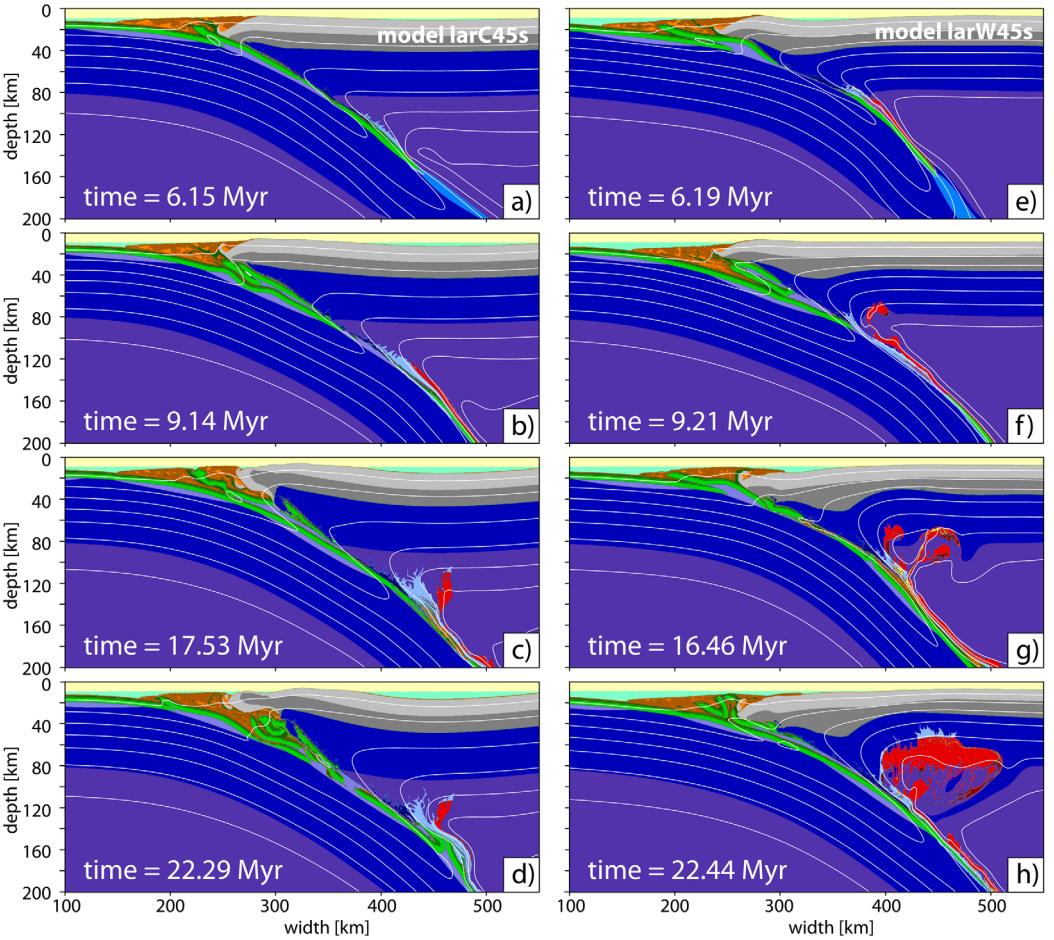

Figure 8. Experiments with large patches of discontinuous slab serpentinization (127.5 km) for (a–d) "cold" and (e-h) "warm" continental geotherms.

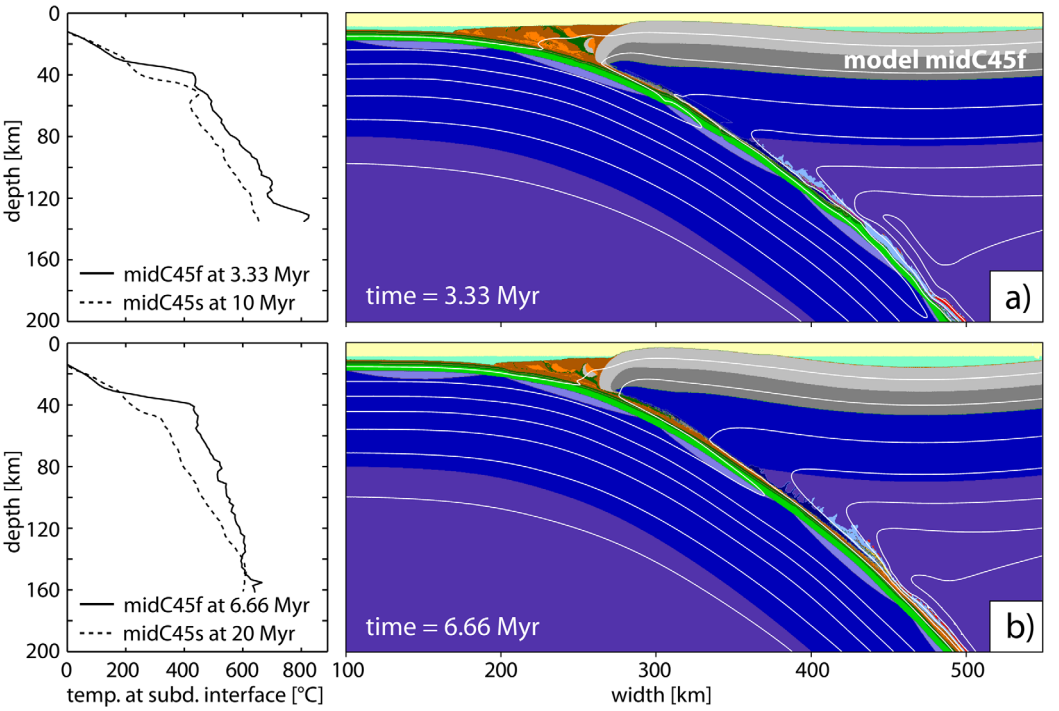

Figure 9. Fast converging (v_x = 12 cm/yr) experiment with discontinuous slab serpentinization after (a) ~3.3 Myr and (b) ~6.6 Myr for a "cold" continental geotherm. Left column: Temperature along the subduction interface (markers with strain rates larger than 10^{-13} s^{-1}).

sedimentary wedge is localized at left pinch-outs of serpentinite patches that goes along with boudinage of crust at the right pinch-out (Figures 8a–8e). The length of the sliced sliver of oceanic crust therefore exhibits a length according to the extent of the serpentinite patch. After ~9 Myr the initially detached sliver has been over-thrusted and sliced (Figures 8b–8f). In "cold" and "warm" models, lower plate serpentinites are incorporated into the upper plate with oceanic crust. After ~17.5 Myr (model larC45s) and ~16.5 Ma (model larW45s), a new oceanic sliver is detached below the sedimentary wedge (Figures 8c–8g). Remnants of earlier detached oceanic slivers are attached to the overriding plate at subcrustal levels. Large parts of the incoming oceanic crust stays attached to the lower plate during subduction, also atop serpentinite patches. After ~22 Myr two different scenarios are observed for "cold" and "warm" experiments. Underplated, internally deformed oceanic crust within the sedimentary wedge can be dragged down into the subduction channel, attached to a larger extend of the accreted sediments (Figure 8d). Contrariwise, the sliced and separated intra-wedge oceanic sliver can be exhumed along corner flow in the accretionary wedge that is forced by underplating (Figure 8h).

3.3.2. Effect of Convergence Velocity

In contrast to the reference model (v_x = 4 cm/yr), numerical experiments with increased convergence velocity of v_x = 12 cm/yr do not exhibit slicing and detachment of oceanic slivers from the downgoing plate (Figure 9). Snapshots after 3.33 Myr and 6.66 Myr of a "cold" experiment with fast compression velocity (model midC45f; Figure 9) exhibit the same amount of shortening as slow models after 10 Myr and 20 Myr, respectively (Figures 5a and 5b). Similar to model midC45s, both erosion of continental crust and subduction of substantial amounts of sediments occur, decreasing the size of the sedimentary accretionary wedge through time (Figure 9). Fast experiments exhibit less hydration and melting of the upper plate mantle than slow models after an equal amount of shortening.

Major differences between fast and slow numerical experiments are expressed by the temperature distribution of the lower plate and along the subduction interface. Plotted isotherms illustrate that the subducting slab of a fast model (v_x = 12 cm/yr) is ~100°C colder than the slab of slow models (v_x = 4 cm/yr) for equal amounts of shortening (Figures 5a, 5b, and 9). This is not surprising as during fast subduction a larger area of cold material is brought into the subduction zone over time. But as a consequence, serpentinite patches within the lower plate mantle are more resistant due to their temperature-dependent power-law viscosity.

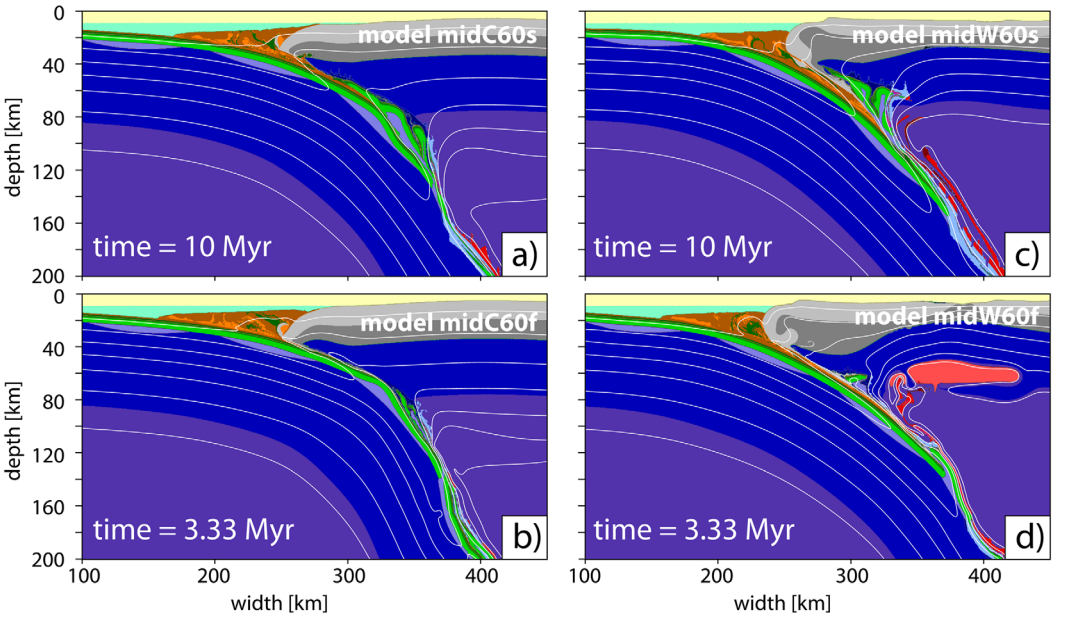

Figure 10. Experiments with discontinuous slab serpentinization and a steep subduction angle ($\alpha = 60°$). (a, c) Slow ($v_x = 4$ cm/yr) and (b, d) fast ($v_x = 12$ cm/yr) experiments with (a, b) "cold" and (c, d) "warm" continental geotherms.

Contrariwise, fast experiments exhibit hotter subduction interfaces than slow models (Figure 9, left column). Temperature differences along the plate interface are in the order of ~100°C reflecting the effect of shear heating along the plate interfaces.

3.3.3. Effect of Slab Dip

Experiments with a subduction angle of 60° (Table 2) exhibit slicing and detachment of oceanic slivers to a certain extent. After 10 Myr, numerical experiments with a slow convergence rate, independent of the continental geotherm, show detachment of large coherent pieces (>20 km) of oceanic crust from the descending plate. These pieces are found folded within serpentinized mantle of the overriding plate (Figures 10a and 10c). Maximum depths of the occurrence of folded slivers in the upper plate are ~120 km for model midC60s and ~80 km for model midW60s. These depths coincide with observed depths for dehydration of serpentinites within the upper plate mantle for models noC45s and noW45s, respectively (Figure 3). Lower plate serpentinites occur within hinges of tightly folded oceanic slivers, being transferred from the lower subducting, onto the upper overriding plate (Figures 10a and10c).

After an equal amount of convergence, fast subduction rate models exhibit much smaller pieces of oceanic crust accreted to the upper plate in contrast to slow models (Figures 10b and 10d). Detached slivers embedded in upper and lower plate serpentinites are ~10 km in length in fast models midC60f and midW60f. Yet their depths vary due upper plate geotherm from ~110 km to ~70 km for "cold" and "warm" cases, respectively (Figures 10b and 10d). These depths are ~10 km shallower than in slow subduction rate experiments, where continental plates had more time to cool along the subduction interface.

4. Discussion

Results presented in this study demonstrate that i) oceanic plate mantle serpentinization prior to subduction plays a key role in detachment oceanic crust from the downgoing plate during subduction, ii) geometry of oceanic mantle serpentinization (continuous versus discontinuous) strongly influences the style of crustal slicing, and iii) that external influences such as convergence velocity, slab angle and continental geotherms affect the degree of interplate coupling and therefore crustal slicing. Generally, the style of oceanic sliver detachment off a subducting plate is dependent on convergence velocity rather than on the temperature distribution in the overriding continental plate. Contrariwise, deformation within the overriding plate is much more a result of its geothermal gradient. "Cold" continents are stiff down to 120 km (Figure 4a and supporting information Figure S4a) and only their tips beneath the sedimentary accretionary wedge are

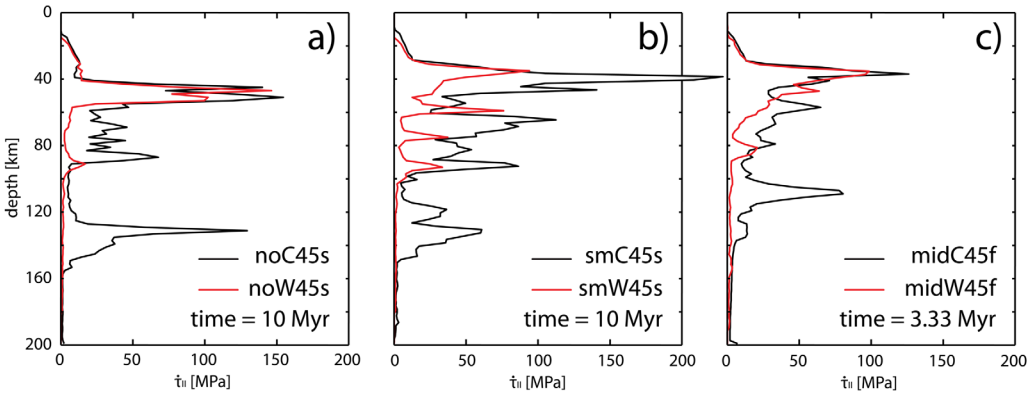

Figure 11. Second invariant of the stress tensor along the subduction interface. (a) Experiments without oceanic plate serpentinization. (b) Experiments with small patches. (c) Experiments with fast convergence. Black lines: "cold" models. Red lines: "warm" models.

dragged toward the subduction zone (Figures 10a and 10b). "Warm" continental plates extend only down to 80 km and their crust is partly decoupled from the mantle (Figure 4b and supporting information Figure S4b). Hence, they exhibit a larger degree of crustal extension and lithospheric thinning (Figures 10c and 10d). Moreover, in context of fast subduction below a "warm" continent, partial decompression melting and thermal upwellings (plumes) in the upper plate mantle due to lithospheric extension accentuate the deformation (Figure 10d).

4.1. Interplate Coupling

The degree of interplate coupling between the upper oceanic crust and the overriding plate has a major influence on slicing of the oceanic crust. Slicing of oceanic crust in subduction zones requires that shear stresses within oceanic crust overcome its yield strength allowing for inward (down-step) migration of the major shear zone below the crust (Figure 6). A down-step of the subduction interface also implies that coupling atop of the sliced crust is stronger than below. If serpentinization of upper oceanic mantle does not take place, mechanical coupling below the oceanic crust is always stronger than above it, mainly due to upper plate serpentinization along the plate interface (Figure 3). In case of oceanic mantle serpentinization, resistance to shear below the subducting crust is strongly reduced.

The degree of coupling atop oceanic crust is illustrated by the second invariant of the stress tensors and the effective viscosity along the plate interface for models that did not exhibit any slicing (Figures 3, 9, 11, and supporting information Figure S5). Stresses along the subduction interface in our experiments are either dependent of the rock's yield strength, in case of plastic/brittle deformation, or due to high strain rates within an otherwise weak material if not at the verge of failure. In all experiments, stresses increase with depth to ~10–20 MPa below the accretionary wedge. Largest stresses occur always at ~40 km depth (Figures 11a–11c), where pore fluids are released and pore pressure diminishes [*Saffer and Tobin*, 2011]. These peaks of large stresses can therefore be related to the downdip limit of seismic coupling along subduction zones, where the upper limit is defined by the smectite to illite transition at 100–150°C and the lower limit by either passing the critical temperature of ~350°C or the presence of subcrustal mantle wedge serpentinites [*Hyndman et al.*, 1997; and references therein]. Peaks of second invariants of stress tensors range in between 100 and 200 MPa (Figure 11) and are on the upper limit of reported strengths of subduction zones in the literature, which are described by shear stresses (10–100 MPa) [*Duarte et al.*, 2015, and references therein]. Lower stress levels below these peaks accord to upper plate serpentinites being the location of main shear deformation (Figure 3, left column). An additional stress peak occurs at ~130 km in "cold" and at ~90 km in "warm" experiments without lower plate serpentinites (Figure 11a) and with small patches of serpentinite (Figure 11b). In models with increased convergence velocity, those peaks are at ~110 km and at ~80 km, respectively (Figure 11c). In terms of stress values, this deep coupling is more intense in "cold" experiments, where stresses are comparable to those at subcrustal levels (Figures 11a–11c, black lines) in contrast to "warm" experiments, where deep stress peaks are low relative to peaks at ~40 km (Figures 11a–11c, red lines). Stress profiles of experiments with small serpentinite patches indicate that location of interplate

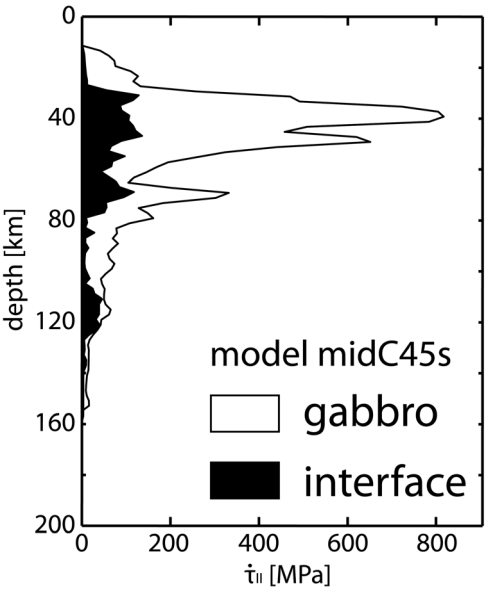

Figure 12. Second invariant of the stress tensor along the subduction interface (white) and averaged values of the second invariant of the stress tensor within lower oceanic crust (black) for the "cold" reference model with discontinuous oceanic mantle serpentinization.

coupling is influenced by the location of patches below the oceanic crust and that stresses along the plate interface can be increased in contrast to models without serpentinization (Figure 11b).

Peak stresses in experiments with a faster convergence rate are ~60–70% of the ones observed in slow models (Figures 11a–11c) as a result of increased shear heating (Figure 9, left column) which leads to lower viscosities along the interface and thus to lower stresses.

Decoupling between crustal slivers and lower mantle and increased strain rates within these decoupling horizons (serpentinites) can lead to stress build up within overlying oceanic crust and subsequent plastic failure and slicing (Figure 6). Obviously, interplate coupling of experiments without serpentinization, with small patches, and with increased convergence velocity was not sufficient to force slicing of oceanic crust. Averaged second invariants of the stress tensor within gabbros of these models are between 0.2 and 0.4 GPa (Figure 7). For the "cold" reference model with medium serpentinite patches, stresses along the plate interface prior to slicing (Figures 6a and 6f; 6.05 Myr) are not larger than in models where slicing is absent (Figures 11 and 12), but averaged stresses within the lower crust are as large as 0.8 GPa and therefore large enough to enforce plastic crustal failure (Figure 12). The stress peak at ~40 km indicates increased compressional stresses at the left pinch-out of the serpentinite patch (Figures 6a and 12). A second peak at ~70 km presents extensional stresses at the right pinch-out of the same patch, leading to the detachment of the crustal sliver along the subduction interface. This underlines that slicing of oceanic slivers depends on both, low coupling below and strong coupling above the subducting crust. Furthermore, results indicate that the determining factor of stress build-up in the lower crust and therefore slicing is the shear force along the subduction interface, i.e., shear stresses acting over a certain distance, which is defined by the length of the serpentine patch. This explains how equal stresses along the interface can lead to larger stresses within the crust if serpentine patches are larger (Figure 12).

4.2. Shallow Versus Deep Slicing and Exhumation of Oceanic Material

Two types of slicing of coherent crustal slivers can be inferred from our model results. Shallow slicing initiates by thrusting of oceanic crust below sedimentary wedges. Oceanic slivers are underplated within the accretionary wedge. Deep slicing initiates at mantle depths within the subduction channel. Whether numerical experiments exhibit shallow, deep or no slicing at all is summarized in Table 2.

Shallow slicing takes place if oceanic mantle serpentinization is continuous (Figure 4) or distributed as large patches below the crust with wavelengths of 127.5 km (Figure 8). There, oceanic crust is thrust at shallow levels below the sedimentary wedge, close to the trench, where confining pressures, and therefore rock strengths, are low (e.g., Figures 4a and 8d). Mechanical coupling below accretionary wedges is very low (<10 MPa) and not sufficient to develop stresses within the crust large enough for plastic failure (Figure 11). Stresses leading to shallow slicing are generated at ~40 km depth within the mantle and distributed along the oceanic crust above decoupling serpentinite. In experiments with continuous serpentinization, the crust is completely decoupled from the oceanic mantle and slicing appears where confining pressures are lowest, i.e., at the trench (Figure 4). For models with large patches of serpentinite, the entrance of the right pinch-out point into the upper plate mantle initiates strong coupling and slicing occurs at the right pinch-out point, where yield strength is lowest (Figure 8). This explains that crustal slices detached above serpentinite patches can later be dragged into the mantle due to areas of strong coupling between decoupling patches. The distance between the trench and the

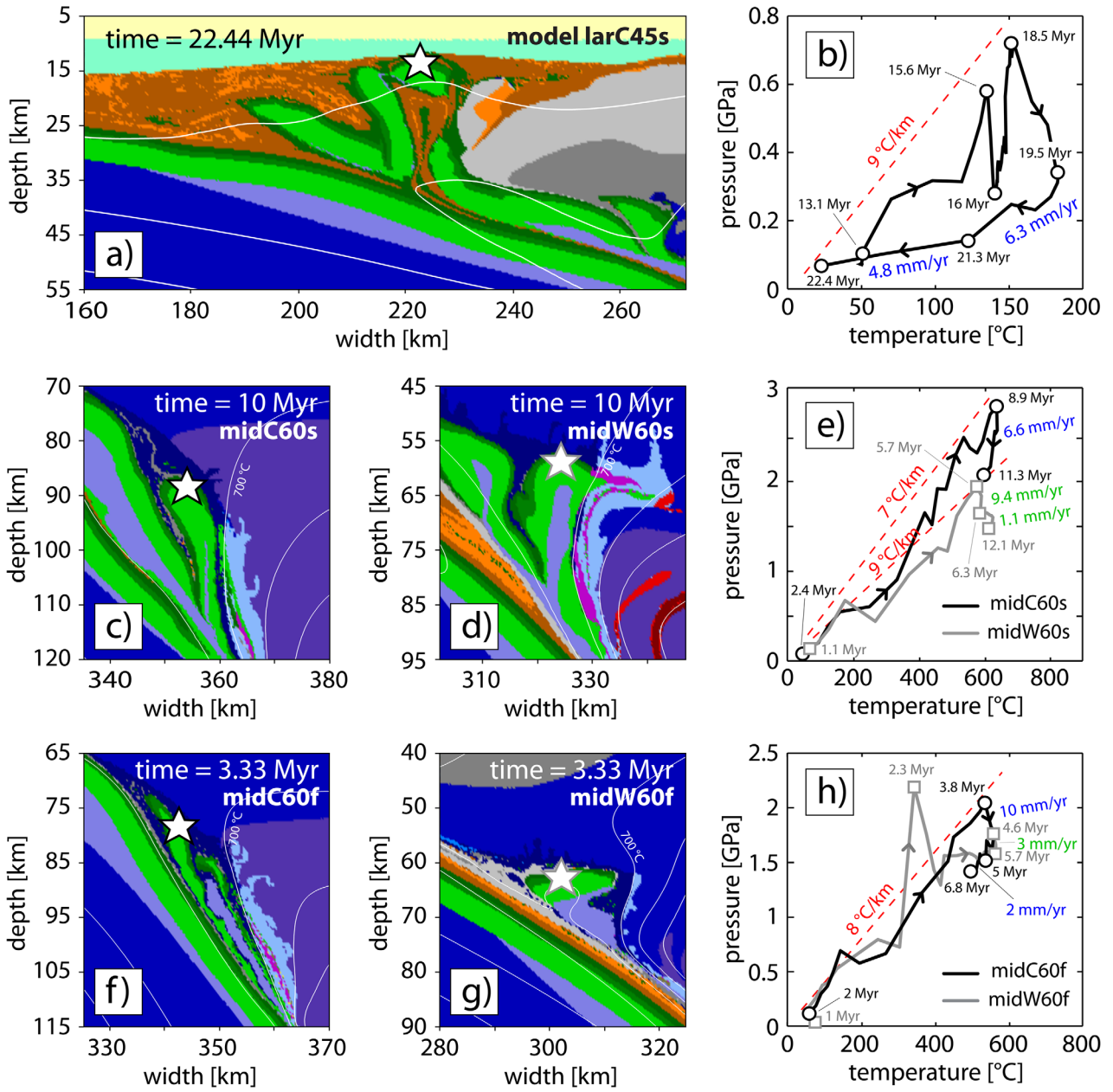

Figure 13. (a) Slicing of complete oceanic crust and exhumation inside the accretionary wedge (Figure 10h). (b) *P-T-t* path of markers indicated by a star in Figure 13a. (c–e) Deep slicing of oceanic slivers in slow convergence velocity (v_x = 4 cm/yr) experiments with (c) a "cold" and (d) a "warm" continental geotherm. (e) *P-T-t* paths of marker patches indicated by stars in Figures 13a and 13b. (f–h) Fast convergence velocity (v_x = 12 cm/yr) experiments with a (f) "cold" and (g) a "warm" continental geotherm. (h) *P-T-t* paths of marker patches indicated by stars in Figures 13f and 13g. Metamorphic heating paths (°C/km) and exhumation rates (mm/yr) are derived dependent on depth instead of pressure.

entrance of the subducting slab to upper mantle depths is around 150 km (Figure 8a). Therefore, models with shorter wavelength patches of serpentinite (<127.5 km) do not exhibit shallow slicing.

The interplay of underplating at the bottom and surface processes at the top of a wedge can cause upward flow of rock that were buried at wedge depths (up to 40 km) and may explain occurrences of oceanic crust and HP tectonic blocks in mélanges (Figure 1) [*Baldwin*, 1996; *Kimura and Ludden*, 1995; *Platt*, 1993]: coherent slivers of oceanic crust including gabbros can be detached at wedge levels and brought to the surface (Figures 8 and 13a). An initially ~100 km long slice of oceanic crust is underthrusted below the wedge, segmented and partly inverted (Figures 8g and 8h). Slivers of oceanic crust are detached along upper oceanic mantle serpentinite patches. Minor amounts of serpentinized slab mantle is attached to sliced oceanic crust

and exhumed with it (Figure 13a). Complete *P-T-t* path of intra-wedge scratched off and exhumed oceanic crust indicate a metamorphic gradient of ~9°C/km. Maximum *P-T* conditions of the investigated crustal patch are 0.7 GPa at 150°C, which is at the edge of the blueschist facies. Rocks are exhumed at rates of 4.8–6.3 mm/yr during ~4 Myr (Figure 13b).

Deep slicing, i.e., detachment of oceanic slivers at mantle depths, depends on (i) the geothermal gradient in the overriding plate, (ii) convergence velocity, (iii) size of serpentinite patches, and (iv) angle of the descending slab. A warmer geothermal gradient diminishes the feasibility of deep slicing as upper plate mantle rocks and plate interface are warmer and thus mechanically weaker (Figure 5). The size of serpentinite patches below the oceanic crust effects the mechanical decoupling between crust and mantle. Larger patches allow stresses in oceanic crust to build up over a larger distance (wavelength of the patch) and thus develop larger stresses at the serpentinite pinch-out. Experiments with small patches (42.5 km) do not exhibit slicing of coherent crustal material (supporting information Figure S5). Experiments with medium sized patches (85 km), slicing is dependent on upper plate temperature, as stated above (Figure 5). Large patches (127.5 km) enhance mainly shallow slicing, although deep thrusting and detachment of dragged down shallow sliced oceanic crust occurs (Figure 8). A steeper slab angle of $\alpha = 60°$ increases the feasibility of deep slicing (Figure 10). However, the extent of sliced material is much less for slowly converging models (Figures 10b and 10d).

Deep slicing predominantly occurs at two distinctive depths within the mantle, given by increased coupling, i.e., stress peaks (Figure 11). In experiments with a subduction angle of $\alpha = 45°$, detachment of oceanic crust from the down-going plate occurs at depths around ~40–60 km (Figure 6). Increased stresses along the interface and deformation within the crust are observed at depths of ~120 km for "cold" and ~80 km for "warm" experiments, respectively. In models with a slab dip angle of $\alpha = 60°$, oceanic crust is detached from the slab at depths, where upper plate serpentinites dehydrate and strength of the mantle increases (Figure 10). Thus, this depth is dependent on the upper plate thermal regime and is at ~120 km in "cold," and at ~80 km in "warm" experiments (Figures 10a and 10c). In fast models, these depths are shifted ~10 km upward due to slightly increased upper mantle temperatures (Figures 10b and 10d). Eventually, this indicates that oceanic crust detached along steeper slabs was brought to deeper mantle levels.

Serpentinization of upper plate mantle above the subduction interface due to dehydration of descending oceanic crust leads to the development the so-called hydrated mantle wedge [*Peacock*, 1993], In case of subduction below a continental lithosphere, the upper limit of the hydrated mantle wedge is defined by the bottom of the continental crust at ~30 km depth (Figure 1). Downward, its extent is restricted by the depth of *P-T*-dependent serpentinite dehydration ~80–120 km [*Schmidt and Poli*, 1998]. The serpentinized mantle wedge provides a volume of low shear stresses and low bulk viscosities coupled to slightly lower densities in contrast to surrounding unaltered mantle rocks. *Schwartz et al*. [2001] stated that the buoyancy induced by density differences between serpentinized and dry mantle wedge can lead to exhumation of HP units. Experiments presented in this study are not supporting that buoyancy forces have a strong impact on exhumation, as basaltic and gabbroic eclogites exhibit densities similar to dry mantle and therefore rather sink within the lighter mantle wedge.

In experiments presented here, slow exhumation of oceanic rocks along the plate interface (channel flow) is induced by forced return flow [*Gerya et al*., 2002]. Dehydration of serpentinites along the ~700°C isotherm strengthens the mantle and establishes a natural backstop preventing material atop the oceanic crust to descend further down into the subduction zone (Figure 13). Underthrusting and detachment of crust pushes earlier accreted material in the direction of least resistance, which is upward within the mantle wedge leading to short-lived pulses of slow exhumation. However, channel flow is restricted to subcrustal levels and cannot bring mantle material toward the surface. Exhumation along crustal depths can be accomplished later during continental collision [*Burov et al*., 2001; *Chemenda et al*., 1995].

P-T-t paths of deeply sliced oceanic crust in experiments with a convergence velocity of $v_x = 4$ cm/yr show metamorphic gradients of 7–10°C/km (Figure 13e). Peak conditions of 2.8 GPa and 630°C occur when the overriding continent is "cold" and thus mantle wedge serpentinite dehydration occurs deeper (~120 km; Figure 13c). The following pulse of exhumation shows rates of 6.6 mm/yr. "Warm" models lead to lower

peak (~2 GPa, 600°C) conditions as the natural backstop occurs at 80–90 km (Figure 13d). Initial exhumation rates of 9.4 mm/yr are induced by folding of the detached sliver. Then, rocks move upward with a velocity of 1.1 mm/yr during ~6 Myr. In fast experiments (v_x= 12 cm/yr), depths of serpentinite dehydration are slightly shallower in contrast to slowly converging models because the slab had less time to cool the overriding plate along the subduction interface after an equal amount of shortening (Figures 13f and 13g). Hence, lower peak *P-T* conditions are reached within sliced oceanic crust (2 GPa, 520°C), except a short-lived, depth-independent peak of 2.3 GPa in the "warm" model, induced by local increase of shear stresses and resulting tectonic overpressure (Figure 13h). Exhumation rates in fast models range from 2 to 3 mm/yr with pulses of up to 10.1 mm/yr (Figure 13h) and are comparable to the ones observed in slow models (Figure 13e). This contradicts findings that showed that exhumation within the subduction channel could be at values of convergence velocities [*Gerya et al*., 2002]. This is because fast experiments accrete less material relative to the amount of incoming crust in contrast to slow models. All detached oceanic slivers consist of gabbros and basalts and are merged between upper and lower plate serpentinites.

4.3. Comparison to Natural Examples

In nature, blueschists and eclogites of oceanic crust are exhumed along different compressional settings related to subduction all over the world [*Agard et al*., 2009; *Maruyama et al*., 1996]. Such crustal slivers can be detached and underplated during arc-continent collision [*Boutelier et al*., 2003], orogenic collision [*Yamato et al*., 2007], but also during ongoing oceanic subduction, as indicated be seismic reflectors [*Vogt and Gerya*, 2014, and references therein]. The timing of exhumation of these metamorphic rocks can be early, intermediate or late, with respect to the subduction cycle [*Agard et al*., 2009]. Late exhumation is often related to continental subduction [*Ernst*, 2001; *Yamato et al*., 2008]. However, this does not necessarily imply that oceanic slivers have not been detached earlier in subduction history and resided in the upper plate mantle wedge until collision. Yet *Agard et al*. [2006] showed that in the Zagros blueschists of intermediate to mafic protoliths buried to depths of 35–50 km were exhumed to midcrustal levels at rates of 1–2 mm/yr ~45 Myr before continental collision during Late Eocene. Their results are comparable to experiments presented here, where detached slivers of oceanic crust are moving upward along the subduction channel (all models with "deep" slicing; Table 2). Exhumation would be ceased as soon as slivers reach crustal levels, which is at 20–30 km depth, depending on the thickness of continental crust.

In general, *P-T-t* paths and other findings presented in this study are in good agreement with published data from oceanic blueschists and eclogites all around the globe [*Agard et al*., 2009, and references therein]:

I. *P-T-t* paths of sliced crust show temperature-depth gradients of ~7–10°C/km, independent of shallow or deep slicing, and also independent of convergence velocity and upper plate initial geothermal gradient (Figure 13). Data compilation of natural examples indicates that metamorphic gradients are usually at the order of 8–10°C/km.
II. Peak pressures of experiments are ~0.7 GPa for shallow, and 2.8 GPa for deep sliced crust (Figure 13). 2.8 GPa are at the upper level of observed pressures of oceanic crust in nature [*Reinecke*, 1991, 1998]. In presented models, such high pressures are a result of the very cold overriding plate, which provides increased serpentinite dehydration depths that define the location of slicing (Figure 13c). Peak pressures are thus dependent on upper plate geothermal gradient. Furthermore, fast convergence velocities reveal lower peak pressures mainly due to the temperature distribution along the subduction zone (Figures 10 and 13). This negative correlation between peak pressures and plate convergence was also shown by *Agard et al*. [2009].
III. Exhumation rates in presented experiments are between 1 and 10 mm/yr, where top velocities (>9 mm/yr) only occur at very short time slots immediately after peak pressure conditions (Figures 13e and 13h). Longer lasting exhumation rates agree very well with rates of 1–5 mm/yr found for natural cases. Shallow sliced show in general faster exhumation rates of >4 mm/yr (Figure 13b).
IV. Several studies pointed out that metamorphic oceanic crust is often associated with serpentinites from the hydrated wedge mantle [*Fitzherbert et al*., 2004; *Scambelluri et al*., 2001], from the upper slab mantle [*Chalot-Prat et al*., 2003; *Li et al*., 2004], or from both [*Hermann et al*., 2000]. In experiments with shallow slicing, lower plate serpentinites are only exhumed with oceanic slivers if the complete crust is disrupted (Figure 13). Upper plate serpentinites are restricted to continental subcrustal levels and are therefore not present. In deep slicing experiments, all oceanic slivers are associated to both, lower plate and upper plate serpentinites (Figure 13).

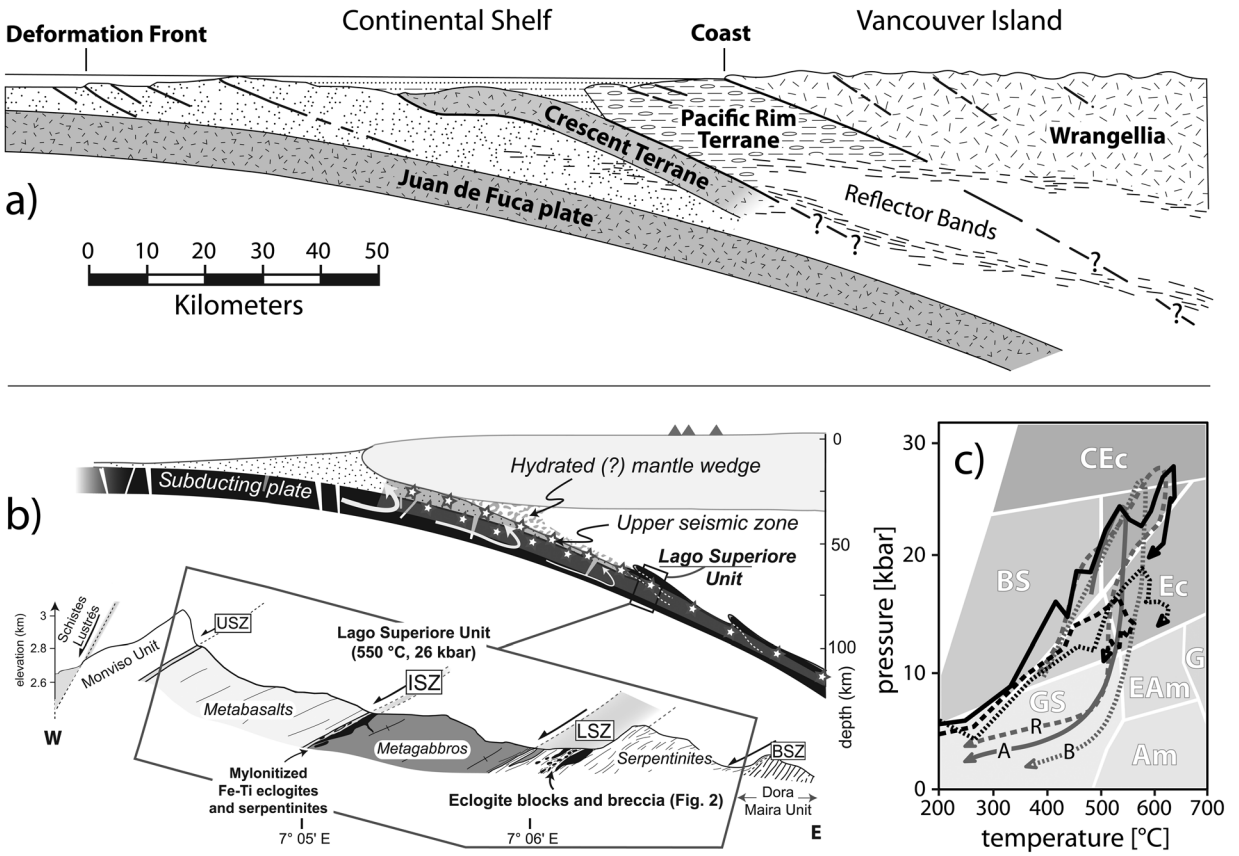

Figure 14. (a) Schematic cross section of the Cascadia subduction zone beneath Vancouver Island (adopted from *Hyndman et al.* [1990]). (b) Schematic view on a subduction zone with deep slicing linked to oceanic sequences and shear zones of the Lago Superiore unit [after *Angiboust et al.*, 2011; *Hacker et al.*, 2003]. (c) Black (full and dashed) lines: *P-T-t* paths obtained in this study according to Figures 13e and 13h). White line: *P-T-t* path of the Lago Superiore unit (AI: *Angiboust et al.*, [2011]). Grey (full and dashed) lines: *P-T-t* paths of the Saas-Zermatt ophiolite (A2: *Angiboust et al.* [2009]; B: *Bucher et al.* [2005]; R: *Reinecke* [1998]).

V. *Ernst* [1988] separated metamorphic exhumation gradients into two end members: i) type I describes mainly adiabatic, or continued heating, decompression paths, and ii) type II nearly coincident retracing of the prograde trajectory. According to model results presented in this study, exhumation of deeply sliced crust would result in type I *P-T* paths (Figures 13e and 13h), because the thermal regime within the subduction channel can be inverted with depth, leading to decompressional heating. Shallow slicing yields rather type II *P-T* paths (Figure 13b).

In the following, two natural cases of shallow and deep slicing are discussed in detail: (i) the oceanic Crescent Terrane accreted along the Cascadia subduction zone at Vancouver Island, and (ii) high-pressure metamorphic oceanic remnants of the Lago Superiore Unit of the Monviso ophiolite, Western Alps (Figure 14).

4.3.1. Crescent Terrane Offshore Vancouver Island

The Crescent Terrane lies beneath the continental shelf west of Vancouver Island and has been identified as a remnant of oceanic crust detached from the Juan de Fuca plate by seismics and borehole drilling [*Hyndman et al.*, 1990; *Narayan et al.*, 2005]. The Crescent Terrane is about 40 km wide and up to 6 km thick and is emplaced beneath the Mesozoic marine sedimentary Pacific Rim Terrane in the east and the recent accretionary prism toward the trench (Figure 14a) [*Hyndman et al.*, 1990]. Onshore correlatives are the Crescent Formation in northern Washington and the Metchosin Complex of southernmost Vancouver Island. The latter comprises a 3 km thick Eocene succession including layered gabbro and sheeted dikes at the base to subaqueous pillow and sheet-flow basalts, minor pyroclastics, and uppermost subaerial arnygdaloidal flows, lacking ultramafic rocks [*Massey*, 1986]. The Crescent Terrane, formed as oceanic crust in a marginal basin [*Wells et al.*, 1984], was first underthrust and then accreted below the North American plate at in the Middle Eocene (48–40 Ma), after a general rearrangement of regional plate motions and near the start of the present phase of

subduction [*Hyndman et al*., 1990; *McCrory and Wilson*, 2013]. Continued underplating triggered onshore uplift and unroofing of the Crescent Terrane marked by rapid cooling [*Groome et al*., 2003]. Metamorphic conditions of these rocks are mainly located in low-grade facies *P-T* fields [*Parsons et al*., 1999], with some excursions into the amphibolite facies [*Timpa et al*., 2005]. However, the existence of sodic amphiboles points to probable high *P-T* metamorphism in the Crescent rocks [*Hirsch and Babcock*, 2009].

Hyndman et al. [1990] proposed two possible scenarios for the accretion of the Crescent Terrane beneath Vancouver Island: i) the complete lithosphere is faulted and the Juan de Fuca plate is then underplating the old lithospheric slab. This is supported by *McCrory and Wilson* [2013], who identified a thermal event associated to a slab tear. Or ii) oceanic crust is detached from the top of the down-going plate with the main locus of subduction unchanged [e.g., *Kimura and Ludden*, 1995]. This is supported by the fact that no ultramafic rocks are associated with the oceanic sliver.

Experiments with large discontinuous patches (127.5 km) of upper oceanic mantle serpentinization resemble observations described above (models larC45s and larW45s; Table 2 and Figures 8c and 8e). These models propose slicing of oceanic crust at wedge levels without major changes in regional subduction dynamics. The fact that the Crescent Terrane was detached and accreted early in the subduction history and since then, no further sliver has been incorporated into the upper plate leads to the conclusion that either coupling along the subduction interface decreased or strong serpentinization of the upper oceanic mantle was restricted to a certain part of the slab. Modeled *P-T* paths of coherent accreted oceanic crust have peak conditions of 0.7 GPa and 150°C which is comparable to reported low-grade metamorphism of Crescent rocks.

4.3.2. Lago Superiore Unit in the Western Alps

The Western Alps result from subduction, accretion and collision between the European and African/Apulian plates from Cretaceous to Oligocene times [*Agard et al*., 2002; *Coward and Dietrich*, 1989]. The internal Western Alps represent a W-verging stack of continental and oceanic nappes. These nappes were formed during subduction and exhumation of the Tethyan seafloor (Liguro-Piemontese domain) and associated European thinned margin below the Apulian plate [*Beltrando et al*., 2010]. Eclogitized oceanic lithosphere of the Liguro-Piemontese domain strikes along 200 km from the Zermatt-Saas area (in the north) to the Monviso area (in the south) [*Angiboust et al*., 2009, 2011]. These metamorphic oceanic remains represent some of the largest and deepest ophiolitic slivers detached and exhumed from a subduction zone [*Bucher et al*., 2005; *Reinecke*, 1998].

The Monviso ophiolite represents the base of the Liguro-Piemontese domain and is separated from the overlying ancient accretionary wedge sediments (Schistes Lustre) and the underlying continental Dora Maira massif (Sampeyre and Dronero units) by extensional shear zones [*Ballevre et al*., 1990; *Blake and Jayko*, 1990]. These shear zones were originally thrust planes, reactivated during the Monviso exhumation [*Philippot and Vanroermund*, 1992]. The Lago Superiore Unit forms the lower oceanic crustal patch of the Monviso ophiolite (Figure 14b). It exhibits a relatively undisturbed section of oceanic lithosphere, composed of metabasalts and associated interpillowmaterial, metadiabases, Fe-Ti metagabbro layers andv calcschists [*Angiboust et al*., 2011], serpentinites derived from hydrothermally altered abyssal peridotites below [*Hattori and Guillot*, 2007]. The Lago Superiore Unit recrystallized within lawsonite eclogite facies close to the coesite stability field in a narrow *P-T* range (500–550°C and 2.2–2.6 GPa) [*Angiboust et al*., 2011].

Experiments with medium sized serpentinite patches exhibit deep slicing of oceanic crust. To reach peak pressures larger than 2 GPa, subduction below a "cold" continent, a slab angle of 60° and slow ($v_x = 4$ cm/yr) convergence velocity is needed (models midC60s and midW60s; Table 2 and Figure 13). Mainly the temperature gradient within the upper continental plate defines the depth of slicing of oceanic material as increased coupling is triggered by the temperature dependent dehydration of upper plate serpentinites (Figure 13c). Experiments presented in this study suggest that metamorphic slices of the Monviso ophiolite could have detached before collision, earlier in the subduction history. This stands not in contradiction with later exhumation associated to buoyant and subducted continental crust. *P-T* paths presented here match very well with observed metamorphic paths of the Lago Superiore and the Saas-Zermatt Units of the Alpine mountain belt (Figure 14c). The very deep slicing and high *P-T* conditions observed in these rocks could be a result of a rather cold continental geotherm of the African/Apulian plate at the time of oceanic subduction.

5. Conclusion

This study investigates the effect of upper oceanic plate mantle serpentinization on slicing of oceanic crust along subduction zones. In case of absence of oceanic mantle serpentinites, most parts of the crust stay attached to the slab mantle and get subducted. Only small portions of altered upper crust return to the surface within the accretionary wedge due to corner flow. Experiments with a continuous serpentinization of upper oceanic mantle exhibit complete accretion (shallow slicing) of oceanic crust before it enters the mantle. Discontinuous, patchy serpentinization of the oceanic mantle lead either to no slicing, shallow slicing at wedge levels, or deep slicing at mantle depths. Whether slicing occurs in the experiments with discontinuous serpentinization, and whether this slicing is at shallow depths or deeper, is dependent on several rheological, mechanical and thermal aspects of the subduction zone:

I. Cooler continental geothermal gradients enhance mechanical coupling and deeper dehydration of serpentinite, favoring deep slicing of oceanic crust.
II. Larger serpentinite patches (170 km) enhance shallow slicing because a larger patch decreases mechanical coupling between the oceanic crust and the oceanic mantle. Furthermore, interplate coupling within the oceanic slab mantle atop a patch occurs when large parts of the oceanic crust atop this patch are still at wedge levels. Experiments with smaller patches (42.5 km) do not exhibit any slicing, as oceanic crustal/mantle decoupling is too weak and stresses built up within the crust are not sufficient for slicing.
III. Faster convergence velocities decrease the slicing potential because shear heating along the plate interface decreases mechanical coupling.
IV. Steeper slab angles enhanced slicing.

Prograde metamorphic gradients are at 7–10°C/km for all experiments. Shallow slices follow rather cooling retrograde paths, deep slices often exhibit decompression paths. Deeply sliced oceanic crust has been observed to move upward within the serpentinized mantle wedge with velocities from 1 to 10 mm/yr, which are comparable to natural observations. Peak metamorphic *P-T* conditions of deep slices match findings from the Lago Superiore and Saas-Zermatt units and show that slicing of crustal slivers can occur independent of continental subduction. Shallow slices have been compared to the Crescent Terrane along the Cascadia subduction zone, stating that serpentinized patches below the oceanic crust are a viable reason for its detachment and accretion onto the upper North American plate.

Appendix A: Grid Spacing, Governing Equations and Numerical Implementation

The Eulerian grid consists of 1060 nodes (600 km wide models: $\alpha = 45°$) or 910 nodes (500 km wide models: $\alpha = 60°$) in *x* direction and 310 nodes in *y* direction. The nodal grid is built to resolve the leftmost 450 km (375 km if $\alpha = 60°$) and top 100 km with 500·500 m cells. Further maximal grid spacing is 1 km in both *x* and *y* direction. Lagrangian marker resolution is based on 4236 (3636 for $\alpha = 60°$) markers in *x* direction and 1545 markers in *y* direction. This results in nodal resolutions of 328600 (282100 $\alpha = 60°$) nodes and 6544620 (5617620 for $\alpha = 60°$) mobile markers.

The mechanical model is based on the equations for mass conservation assuming incompressibility

$$\frac{\partial u_i}{\partial x_i} = 0 \tag{A1}$$

and the conservation of momentum, the Stokes equation

$$-\frac{\partial P}{\partial x_i} + \frac{\partial \tau_{ij}}{\partial x_j} = \rho g_i \tag{A2}$$

where

$$\tau_{ij} = 2\eta \dot{\varepsilon}_{ij} \tag{A3}$$

and

$$\dot{\varepsilon}_{ij} = \frac{1}{2}\left(\frac{\partial u_i}{\partial x_j} + \frac{\partial u_j}{\partial x_i}\right) \tag{A4}$$

P is pressure, u_i the velocity ($u_1 = u_x$, $u_2 = u_y$), x_i the spatial coordinates ($x_1 = x$, $x_2 = y$), τ_{ij} the deviatoric stress tensor, ρ the density, g_i the gravitational acceleration ($g_1 = 0$, $g_2 = 9.81$ m/s^2), η the viscosity and $\dot{\varepsilon}_{ij}$ the strain rate tensor.

Effective creep viscosities are depending on temperature and stress due to experimentally determined flow laws (Table 1). Diffusion creep (η_{diff}) and dislocation creep (η_{disl}) are accounted for all rock types following *Karato and Li* [1992]:

$$\eta_{diff} = 0.5 \frac{A_D}{S^{(n-1)}} e^{\frac{(E+V \cdot P)}{RT}} \tag{A5}$$

$$\eta_{disl} = 0.5 \cdot A_D^{\left(\frac{1}{n}\right)} \cdot \dot{\varepsilon}_{II}^{\left(\frac{1}{n}-1\right)} e^{\frac{(E+V \cdot P)}{nRT}} \tag{A6}$$

$$\eta_{creep} = \left(\frac{1}{\eta_{diff}} + \frac{1}{\eta_{disl}}\right)^{-1} \tag{A7}$$

where

$$\dot{\varepsilon}_{ij} = \sqrt{\frac{1}{2}\dot{\varepsilon}_{ij}^2}, \tag{A8}$$

A_D describes the preexponential factor, n is the power-law exponent, E is activation energy, V is the activation volume, S is a stress factor for diffusion creep (30,000 Pa) and R is the gas constant.

If differential stresses calculated in equation (A3) exceed the yield stress, plastic failure follows the Drucker-Prager yield criterion with the plastic yield function F (equation (A11)), depending on the second invariant of the stress tensor τ_{II} and the yield stress σ_y

$$F = \tau_{II} - \sigma_y \tag{A9}$$

where

$$\tau_{II} = \sqrt{\frac{1}{2}\tau_{ij}^2} \tag{A10}$$

and

$$\sigma_y = P \cdot \sin\varphi \cdot (1-\lambda) + C \cdot \cos\varphi \tag{A11}$$

C is the cohesion, φ the friction angle and λ the fluid pressure ratio.

Effective creep viscosities η_{creep} are decreased depending on the second invariant of the strain rate tensor $\dot{\varepsilon}_{II}$ and the yield stress σ_y until the maximum stresses are at the yield stress ($F = 0$), according to

$$\eta_{vp} = \frac{\sigma_y}{2\dot{\varepsilon}_{II}} \tag{A12}$$

and η_{vp} is the effective viscosity corrected for plasticity. Lower and upper viscosity cutoffs are 10^{17} and 10^{24} Pa·s.

In the same framework, solving the Lagrangian form of the energy equation provides temperature T and is given by

$$\rho C_p \left(\frac{DT}{Dt}\right) = -\frac{\partial q_i}{\partial x_i} + H_r + H_a + H_s \tag{A13}$$

where ρ is density, C_p isobaric heat capacity, T temperature, t time. Furthermore, vertical and horizontal heat fluxes are described following

$$q_i = -k(T,P) \cdot \frac{\partial T}{\partial x_i} \tag{A14}$$

where k is the thermal conductivity coefficient depending on temperature and pressure (Table 1) [*Clauser and Huenges*, 1995; *Hofmeister*, 1999]. Heat sources comprise radioactive heating (H_r), simplified adiabatic heating (H_a) and shear heating (H_s) according to *Gerya and Yuen* [2003].

Acknowledgments
We thank two anonymous reviewers and Thorsten Becker for their valuable comments on the manuscript. The research leading to these results has received funding from the People Programme (Marie Curie Actions) of the European Union's Seventh Framework Programme FP7/2007-2013/under REA grant agreement 604713. Data presented in this work are available to anyone upon request from the corresponding author.

References

Agard, P., P. Monie, L. Jolivet, and B. Goffe (2002), Exhumation of the Schistes Lustres complex: In situ laser probe Ar-40/Ar-39 constraints and implications for the Western Alps, *J. Metamorph. Geol.*, *20*(6), 599–618.

Agard, P., P. Monie, W. Gerber, J. Omrani, M. Molinaro, B. Meyer, L. Labrousse, B. Vrielynck, L. Jolivet, and P. Yamato (2006), Transient, synobduction exhumation of Zagros blueschists inferred from P-T, deformation, time, and kinematic constraints: Implications for Neotethyan wedge dynamics, *J. Geophys. Res.*, *111*, B11401, doi:10.1029/2005JB004103.

Agard, P., P. Yamato, L. Jolivet, and E. Burov (2009), Exhumation of oceanic blueschists and eclogites in subduction zones: Timing and mechanisms, *Earth Sci. Rev.*, *92*(1–2), 53–79.

Amato, J. M., C. M. Johnson, L. P. Baumgartner, and B. L. Beard (1999), Rapid exhumation of the Zermatt-Saas ophiolite deduced from high-precision Sm-Nd and Rb-Sr geochronology, *Earth Planet. Sci. Lett.*, *171*(3), 425–438.

Angiboust, S., and P. Agard (2010), Initial water budget The key to detaching large volumes of eclogitized oceanic crust along the subduction channel?, *Lithos*, *120*(3–4), 453–474.

Angiboust, S., P. Agard, L. Jolivet, and O. Beyssac (2009), The Zermatt-Saas ophiolite: The largest (60-km wide) and deepest (c. 70-80 km) continuous slice of oceanic lithosphere detached from a subduction zone?, *Terra Nova*, *21*(3), 171–180.

Angiboust, S., P. Agard, H. Raimbourg, P. Yamato, and B. Huet (2011), Subduction interface processes recorded by eclogite-facies shear zones (Monviso, W. Alps), *Lithos*, *127*(1–2), 222–238.

Angiboust, S., S. Wolf, E. Burov, P. Agard, and P. Yamato (2012), Effect of fluid circulation on subduction interface tectonic processes: Insights from thermo-mechanical numerical modelling, *Earth Planet. Sci. Lett.*, *357*, 238–248.

Arculus, R. J., H. Lapierre, and E. Jaillard (1999), Geochemical window into subduction and accretion processes: Raspas metamorphic complex, Ecuador, *Geology*, *27*(6), 547–550.

Austrheim, H., and T. M. Boundy (1994), Pseudotachylytes generated during seismic faulting and eclogitization of the deep crust, *Science*, *265*(5168), 82–83.

Baldwin, S. L. (1996), Contrasting P-T-t histories for Blueshists from the Western Baja Terrane and the Aegean: Effects of synsubduction exhumation and backarc extension, in *Subduction: Top to Bottom*, edited by B. E. Bebout et al., pp. 135–141, AGU, Washington, D. C.

Ballevre, M., Y. Lagabrielle, and O. Merle (1990), Tertiary ductile normal faulting as a consequence of lithospheric stacking in the Western Alps, *Mem. Soc. Geol. Fr.*, *156*, 227–236.

Beltrando, M., D. Rubatto, and G. Manatschal (2010), From passive margins to orogens: The link between ocean-continent transition zones and (ultra)high-pressure metamorphism, *Geology*, *38*(6), 559–562.

Blake, M. C., and A. S. Jayko (1990), Uplift of very high-pressure rocks in the Western Alps––Evidence for structural attenuation along low-angle faults, *Mem. Soc. Geoi. Fr.*, *156*, 237–246.

Boutelier, D., A. Chemenda, and J.-P. Burg (2003), Subduction versus accretion of intra-oceanic volcanic arcs: Insight from thermo-mechanical analogue experiments, *Earth Planet. Sci. Lett.*, *212*, 31–45.

Bucher, K., Y. Fazis, C. De Capitani, and R. Grapes (2005), Blueschists, eclogites, and decompression assemblages of the Zermatt-Saas ophiolite: High-pressure metamorphism of subducted Tethys lithosphere, *Am. Mineral.*, *90*(5–6), 821–835.

Burov, E., and P. Yamato (2008), Continental plate collision, P-T-t-z conditions and unstable vs. stable plate dynamics: Insights from thermo-mechanical modelling, *Lithos*, *103*(1–2), 178.

Burov, E., L. Jolivet, L. Le Pourhiet, and A. Poliakov (2001), A thermomechanical model of exhumation of high pressure (HP) and ultra-high pressure (UHP) metamorphic rocks in Alpine-type collision belts, *Tectonophysics*, *342*(1–2), 113–136.

Cann, J. R., D. K. Blackman, D. K. Smith, E. McAllister, B. Janssen, S. Mello, E. Avgerinos, A. R. Pascoe, and J. Escartin (1997), Corrugated slip surfaces formed at ridge-transform intersections on the Mid-Atlantic Ridge, *Nature*, *385*(6614), 329–332.

Cannat, M., et al. (1995), Thin crust, ultramafic exposures, and rugged faulting patterns at mid-Atlantic Ridge (22-degrees 24-degrees-N), *Geology*, *23*(1), 49–52.

Chalot-Prat, F., J. Ganne, and A. Lombard (2003), No significant element transfer from the oceanic plate to the mantle wedge during subduction and exhumation of the Tethys lithosphere (Western Alps), *Lithos*, *69*(3–4), 69–103.

Chemenda, A. I., M. Mattauer, J. Malavieille, and A. N. Bokun (1995), A mechanism for syn-collisional rock exhumation and associated normal faulting––Results from physical modeling, *Earth Planet. Sci. Lett.*, *732*(1–4), 225–232.

Chopin, C. (1984), Coesite and pure pyrope in high-grade Blueschists of the Western Alps––A 1st record and some consequences, *Contrib. Mineral. Petrol.*, *86*(2), 107–118.

Clauser, C., and E. Huenges (1995), Thermal conductivity of rocks and minerals, in *Rock Physics and Phase Relations*, edited by T. J. Ahrens, pp. 105–126, AGU, Washington, D. C.

Cloetingh, S. A. P. L., M. J. R. Wortel, and N. J. Vlaar (1982), Evolution of passive continental margins and initiation of subduction zones, *Nature*, *297*(5862), 139–142.

Cloos, M., and R. L. Shreve (1988a), Subduction-channel model of prism accretion, melange formation, sediment subduction, and subduction erosion at convergent plate margins. 2. Implications and discussion, *Pure Appl. Geophys.*, *128*(3–4), 501–545.

Cloos, M., and R. L. Shreve (1988b), Subduction-channel model of prism accretion, melange formation, sediment subduction, and subduction erosion at convergent plate margins. 1. Background and description, *Pure Appl. Geophys.*, *128*(3–4), 455–500.

Connolly, J. A. D. (2005), Computation of phase equilibria by linear programming: A tool for geodynamic modeling and its application to subduction zone decarbonation, *Earth Planet. Sci. Lett.*, *236*(1–2), 524–541.

Connolly, J. A. D., and K. Petrini (2002), An automated strategy for calculation of phase diagram sections and retrieval of rock properties as a function of physical conditions, *J. Metamorph. Geol.*, *20*(1), 697–708.

Conrad, C. P., S. Bilek, and C. Lithgow-Bertelloni (2004), Great earthquakes and slab pull: Interaction between seismic coupling and plate-slab coupling, *Earth Planet. Sci. Lett.*, *218*(1–2), 109–122.

Coward, M. P., and D. Dietrich (1989), Alpine tectonics––An overview, in *Alpine Tectonics*, edited by M. P. Coward, D. Dietrich, and R. G. Park, pp. 1–29, Geol. Soc., London, U. K.

Crameri, F., H. Schmeling, G. J. Golabek, T. Duretz, R. Orendt, S. J. H. Buiter, D. A. May, B. J. P. Kaus, T. V. Gerya, and P. J. Tackley (2012), A comparison of numerical surface topography calculations in geodynamic modelling: An evaluation of the sticky air' method, *Geophys. J. Int.*, *189*(1), 38–54.

Dobrzhinetskaya, L., H. W. Green, and S. Wang (1996), Alpe Arami: A peridotite massif from depths of more than 300 kilometers, *Science*, *277*(5257), 1841–1845.

Duarte, J. C., W. P. Schellart, and A. R. Cruden (2015), How weak is the subduction interface?, *Geophys. Res. Lett.*, *42*, 2664–2673, doi:10.1002/2014GL062876.

Ernst, W. G. (1988), Tectonic history of subduction zones inferred from retrograde Blueschist P-T paths, *Geology*, *76*(12), 1081–1084.
Ernst, W. G. (2001), Subduction, ultrahigh-pressure metamorphism, and regurgitation of buoyant crustal slices––Implications for arcs and continental growth, *Phys. Earth Planet. Inter., 727*(1–4), 253–275.
Escartin, J., G. Hirth, and B. Evans (1997), Effects of serpentinization on the lithospheric strength and the style of normal faulting at slow-spreading ridges, *Earth Planet. Sci. Lett.*, *757*(3–4), 181–189.
Faccenda, M., T. V. Gerya, and L. Burlini (2009), Deep slab hydration induced by bending-related variations in tectonic pressure, *Nat. Geosci.*, *2*(11), 790–793.
Faccenda, M., T. V. Gerya, N. S. Mancktelow, and L. Moresi (2012), Fluid flow during slab unbending and dehydration: Implications for intermediate-depth seismicity, slab weakening and deep water recycling, *Geochem. Geophys. Geosyst.*, *13*, Q01010, doi:10.1029/2011GC003860.
Fitzherbert, J. A., G. L. Clarke, B. Marmo, and R. Powell (2004), The origin and P-T evolution of peridotites and serpentinites of NE New Caledonia: Prograde interaction between continental margin and the mantle wedge, *J. Metamorph. Geol.*, *22*(4), 327–344.
Frey, M. (1987), *Low Temperature Metamorphism*, 351 pp., Blackie Acad. and Prof., Glasgow, U. K.
Fruh-Green, G., A. Plas, and C. Lecuyer (1996), Petrologic and stable isotope constraints on hydrothermal alteration and serpentinization of the EPR shallow mantle at hess deep (site 895), *Proc. Ocean Drill. Program Sci. Results*, *747*, 255.
Fryer, P. (2002), Recent studies of serpentinite occurrences in the oceans: Mantle-ocean interactions in the plate tectonic cycle, *Chemie Der Erde Geochemistry*, *62*(4), 257–302.
Gerya, T. V., and F. I. Meilick (2011), Geodynamic regimes of subduction under an active margin: Effects of rheological weakening by fluids and melts, *J. Metamorph. Geol.*, *29*(1), 7–31.
Gerya, T. V., and D. A. Yuen (2003), Rayleigh-Taylor instabilities from hydration and melting propel 'cold plumes' at subduction zones, *Earth Planet. Sci. Lett., 272*(1–2), 47–62.
Gerya, T. V., B. Stockhert, and A. L. Perchuk (2002), Exhumation of high-pressure metamorphic rocks in a subduction channel: A numerical simulation, *Tectonics*, *27*(6), 1056, doi:10.1029/2002TC001406.
Gerya, T. V., J. A. D. Connolly, D. A. Yuen, W. Gorczyk, and A. M. Capel (2006), Seismic implications of mantle wedge plumes, *Phys. Earth Planet. Inter.*, *756*(1–2), 59–74.
Gorczyk, W., S. Guillot, T. V. Gerya, and K. Hattori (2007a), Asthenospheric upwelling, oceanic slab retreat, and exhumation of UHP mantle rocks: Insights from Greater Antilles, *Geophys. Res. Lett., 34*, L21309, doi:10.1029/2007GL031059.
Gorczyk, W., T. V. Gerya, J. A. D. Connolly, J. P. Burg, and D. A. Yuen (2007b), Melting and mixing processes in mantle wedges, *Geochim. Cosmochim. Acta*, *77*(15), A346–A346.
Gosh, R. C., S. Tanaka, and A. Toda (2010), Application of a deconvolution method to construct aqueous phase diagram, *Thermochimica Acta*, *500*(1–2), 100–105.
Gressier, J. B., R. Mourgues, L. Bodet, J. Y. Matthieu, O. Galland, and P. Cobbold (2010), Control of pore fluid pressure on depth of emplacement of magmatic sills: An experimental approach, *Tectonophysics*, *489*(1–4), 1–13.
Groome, W. G., D. J. Thorkelson, R. M. Friedman, J. K. Mortensen, N. W. D. Massey, D. D. Marshall, and P. W. Layer (2003), Magmatic and tectonic history of the Leech River Complex, Vancouver Island, British Columbia: Evidence for ridge-trench intersection and accretion of the Crescent Terrane, in *Geology of a Transpressional Orogen Developed During Ridge-Trench Interaction Along the North Pacific Margin*, edited by V. B. Sisson, S. M. Roeske and T. L. Pavlis, pp. 327–353, Geol. Soc. Am., Boulder, Colo.
Guillot, S., K. H. Hattori, J. de Sigoyer, T. Nagler, and A. L. Auzende (2001), Evidence of hydration of the mantle wedge and its role in the exhumation of eclogites, *Earth Planet. Sci. Lett.*, *193*(1–2), 115–127.
Guillot, S., K. Hattori, P. Agard, S. Schwartz, and O. Vidal (2009), Exhumation Processes in Oceanic and Continental Subduction Contexts: A Review, in *Front Earth Sci Ser*, edited by S. Lallemand and F. Funiciello, pp. 175–205, Springer, Berlin, Heidelberg.
Guillot, S., S. Schwartz, B. Reynard, P. Agard, and C. Prigent (2015), Tectonic significance of serpentinites, *Tectonophysics*, *646*, 1–19.
Gurnis, M. (1992), Rapid continental subsidence following the initiation and evolution of subduction, *Science*, *255*(5051), 1556–1558.
Hacker, B. R., S. M. Peacock, G. A. Abers, and S. D. Holloway (2003), Subduction factory––2. Are intermediate-depth earthquakes in subducting slabs linked to metamorphic dehydration reactions?, *J. Geophys. Res.*, *708*(B1), 2030, doi:10.1029/2001JB001129.
Hattori, K. H., and S. Guillot (2007), Geochemical character of serpentinites associated with high- to ultrahigh-pressure metamorphic rocks in the Alps, Cuba, and the Himalayas: Recycling of elements in subduction zones, *Geochem. Geophys. Geosyst.*, *8*, Q09010, doi:10.1029/2007GC001594.
Hermann, J., O. Muntener, and M. Scambelluri (2000), The importance of serpentinite mylonites for subduction and exhumation of oceanic crust, *Tectonophysics*, *327*(3–4), 225–238.
Heuret, A., and S. Lallemand (2005), Plate motions, slab dynamics and back-arc deformation, *Phys. Earth Planet. Inter.*, *149*(1–2), 31–51.
Hilairet, N., B. Reynard, Y. B. Wang, I. Daniel, S. Merkel, N. Nishiyama, and S. Petitgirard (2007), High-pressure creep of serpentine, interseismic deformation, and initiation of subduction, *Science*, *318*(5858), 1910–1913.
Hirsch, D. M., and R. S. Babcock (2009), Spatially heterogeneous burial and high-P/T metamorphism in the Crescent Formation, Olympic Peninsula, Washington, *Am. Mineral.*, *94*(8–9), 1103–1110.
Hofmeister, A. M. (1999), Mantle values of thermal conductivity and the geotherm from phonon lifetimes, *Science*, *285*(5408), 1699–1706.
Hutnak, M., A. T. Fisher, R. Harris, C. Stein, K. Wang, G. Spinelli, M. Schindler, H. Villinger, and E. Silver (2008), Large heat and fluid fluxes driven through mid-plate outcrops on ocean crust, *Nat. Geosci.*, *1*(9), 611–614.
Hyndman, R. D., C. J. Yorath, R. M. Clowes, and E. E. Davis (1990), The Northern Cascadia subduction zone at Vancouver Island––Seismic structure and tectonic history, *Can. J. Earth Sci.*, *27*(3), 313–329.
Hyndman, R. D. (1995), The Lithoprobe corridor across the Vancouver Island continental margin: The structural and tectonic consequences of subduction, *Can J Earth Sci*, *32*(10), 1777–1802.
Hyndman, R. D., M. Yamano, and D. A. Oleskevich (1997), The seismogenic zone of subduction thrust faults, *Island Arc*, *6*(3), 244–260.
Ivandic, M., I. Grevemeyer, J. Bialas, and C. J. Petersen (2010), Serpentinization in the trench-outer rise region offshore of Nicaragua: Constraints from seismic refraction and wide-angle data, *Geophys. J. Int.*, *180*(3), 1253–1264.
Iyer, K., L. H. Rupke, and J. P. Morgan (2010), Feedbacks between mantle hydration and hydrothermal convection at ocean spreading centers, *Earth Planet. Sci. Lett.*, *296*(1–2), 34–44.
Janecky, D. R., and W. E. Seyfried (1986), Hydrothermal serpentinization of peridotite within the oceanic-crust––Experimental investigations of mineralogy and major element chemistry, *Geochim. Cosmochim. Acta*, *50*(1), 1357–1378.
Kanamori, H., D. L. Anderson, and T. H. Heaton (1998), Frictional melting during the rupture of the 1994 Bolivian earthquake, *Science*, *279*(5352), 839–842.
Karato, S., and P. Li (1992), Diffusion creep in perovskite––Implications for the rheology of the lower mantle, *Science*, *255*(5049), 1238–1240.

Kelley, D. S., et al. (2001), An off-axis hydrothermal vent field near the Mid-Atlantic Ridge at 30 degrees N, *Nature*, *472*(6843), 145–149.
Kimura, G., and J. Ludden (1995), Peeling oceanic-crust in subduction zones, *Geology, 25*(3), 217–220.
Li, X. P., M. Rahn, and K. Bucher (2004), Serpentinites of the Zermatt-Saas ophiolite complex and their texture evolution, *J. Metamorph. Geol.*, *22*(3), 159–177.
Martin, B., and W. S. Fyfe (1970), Some experimental and theoretical observations on kinetics of hydration reactions with particular reference to serpentinization, *Chem. Geol.*, *6*(3), 185.
Maruyama, S., J. G. Liou, and M. Terabayashi (1996), Blueschist and eclogites of the world and their exhumation, *Int. Geol. Rev.*, *38*, 485–594.
Massey, N. W. D. (1986), Metchosin igneous complex, Southern Vancouver Island––Ophiolite stratigraphy developed in an emergent island setting, *Geology*, *74*(7), 602–605.
McCaig, A. M., R. A. Cliff, J. Escartin, A. E. Fallick, and C. J. MacLeod (2007), Oceanic detachment faults focus very large volumes of black smoker fluids, *Geology*, *55*(10), 935–938.
McCrory, P. A., and D. S. Wilson (2013), A kinematic model for the formation of the Siletz-Crescent forearc terrane by capture of coherent fragments of the Farallon and Resurrection plates, *Tectonics*, *32*, 718–736, doi:10.1002/tect.20045.
Monie, P., and P. Agard (2009), Coeval blueschist exhumation along thousands of kilometers: Implications for subduction channel processes, *Geochem. Geophys. Geosyst.*, *10*, Q07002, doi:10.1029/2009GC002428.
Moore, C. J., and H. Tobin (1997), Estimated fluid pressures of the Barbados accretionary prism and adjacent sediments, in *Proceedings of the Ocean Drilling Program, Scientific Results*, edited by T. H. Shipley et al., pp. 229–238, Ocean Drill. Program, College Station, Tex.
Moreno, M., C. Haberland, O. Oncken, A. Rietbrock, S. Angiboust, and O. Heidbach (2014), Locking of the Chile subduction zone controlled by fluid pressure before the 2010 earthquake, *Nat. Geosci.*, *7*(4), 292–296.
Muller, M. R., C. J. Robinson, T. A. Minshull, R. S. White, and M. J. Bickle (1997), Thin crust beneath ocean drilling program borehole 73 5B at the Southwest Indian Ridge?, *Earth Planet. Sci. Lett.*, *748*(1–2), 93–107.
Narayan, Y. R., C. R. Barnes, and M. J. Johns (2005), Taxonomy and biostratigraphy of Cenozoic foraminifers from Shell Canada wells, Tofino Basin, offshore Vancouver Island, British Columbia, *Micropaleontology*, *57*(2), 101–167.
Nikolaeva, K., T. V. Gerya, and F. O. Marques (2010), Subduction initiation at passive margins: Numerical modeling, *J. Geophys. Res.*, *115*, B03406, doi:10.1029/2009JB006549.
Parsons, T., R. E. Wells, M. A. Fisher, E. Flueh, and U. S. ten Brink (1999), Three-dimensional velocity structure of Siletzia and other accreted terranes in the Cascadia forearc of Washington, *J Geophys Res.*, *704*(B8), 18,015–18,039.
Peacock, S. M. (1993), Large-scale hydration of the lithosphere above subducting slabs, *Chem. Geol., 708*(1–4), 49–59.
Peacock, S. M. (2001), Are the lower planes of double seismic zones caused by serpentine dehydration in subducting oceanic mantle?, *Geology*, *29*(4), 299–302.
Perry, E., and J. Hower (1970), Burial diagenesis in Gulf Coast pelitic sediments, *Clays Clay Miner.*, 78(3), 165.
Philippot, P., and H. L. M. Vanroermund (1992), Deformation processes in eclogitic rocks––Evidence for the rheological delamination of the oceanic-crust in deeper levels of subduction zones, *J. Struct. Geol.*, 74(8–9), 1059–1077.
Platt, J. P. (1993), Exhumation of high-pressure rocks––A review of concepts and processes, *Terra Nova*, *5*(2), 119–133.
Plunder, A., P. Agard, C. Chopin, A. Pourteau, and A. Okay (2015), Accretion, underplating and exhumation along a subduction interface: From subduction initiation to continental subduction (Tav§anh zone, W. Turkey), *Lithos*, *226*, 233–254.
Ranalli, G. (1995), *Rheology of the Earth*, 413 pp., Chapman and Hall, London, U. K.
Ranero, C. R., J. P. Morgan, K. McIntosh, and C. Reichert (2003), Bending-related faulting and mantle serpentinization at the Middle America trench, *Nature*, *425*(6956), 367–373.
Ranero, C. R., I. Grevemeyer, H. Sahling, U. Barckhausen, C. Hensen, K. Wallmann, W. Weinrebe, P. Vannucchi, R. von Huene, and K. McIntosh (2008), Hydrogeological system of erosional convergent margins and its influence on tectonics and interplate seismogenesis, *Geochem. Geophys. Geosyst.*, *9*, Q03S04, doi:10.1029/2007GC001679.
Reinecke, T. (1991), Very-high-pressure metamorphism and uplift of coesite-bearing metasediments from the Zermatt-Saas Zone, Western Alps, *Eur. J. Mineral.*, *5*(1), 7–17.
Reinecke, T. (1998), Prograde high- to ultrahigh-pressure metamorphism and exhumation of oceanic sediments at Lago di Cignana, Zermatt-Saas Zone, western Alps, *Lithos*, *42*(3–4), 147–189.
Ruh, J. B., B. J. P. Kaus, and J. P. Burg (2012), Numerical investigation of deformation mechanics in fold-and-thrust belts: Influence of rheology of single and multiple decollements, *Tectonics*, *31*, TC3005, doi:10.1029/2011TC003047.
Saffer, D. M., and H. J. Tobin (2011), Hydrogeology and mechanics of subduction zone forearcs: Fluid flow and pore pressure, *Annu. Rev. Earth Planet. Sci.*, *39*, 157–186.
Scambelluri, M., P. Bottazzi, V. Trommsdorff, R. Vannucci, J. Hermann, M. T. Gomez-Pugnaire, and V. L. S. Vizcaino (2001), Incompatible element-rich fluids released by antigorite breakdown in deeply subducted mantle, *Earth Planet. Sci. Lett.*, *192*(3), 457–470.
Schenk, O., and K. Gartner (2004), Solving unsymmetric sparse systems of linear equations with PARDISO, *Future Gener. Comput. Syst.*, *20*(3), 475–487.
Schenk, O., and K. Gartner (2006), On fast factorization pivoting methods for sparse symmetric indefinite systems, *Electron. Trans. Numer. Anal.*, *23*, 158–179.
Schmidt, M. W., and S. Poli (1998), Experimentally based water budgets for dehydrating slabs and consequences for arc magma generation, *Earth Planet. Sci. Lett., 765*(1–4), 361–379.
Schubert, G., C. Froidevaux, and D. A. Yuen (1976), Oceanic lithosphere and asthenosphere––Thermal and mechanical structure, *J. Geophys. Res.*, *87*(20), 3525–3540.
Schwartz, S., P. Allemand, and S. Guillot (2001), Numerical model of the effect of serpentinites on the exhumation of eclogitic rocks: Insights from the Monviso ophiolitic massif (Western Alps), *Tectonophysics*, *342*(1–2), 193–206.
Syracuse, E. M., P. E. van Keken, and G. A. Abers (2010), The global range of subduction zone thermal models, *Phys. Earth Planet. Inter., 783*(1-2), 73–90.
Tartarotti, P., S. Martin, and R. Polino (1986), Geological data about the ophiolitic sequences in the St. Marcel valley (Aosta Valley), *Ofioliti*, *3*, 343–346.
Timpa, S., K. M. Gillis, and D. Canil (2005), Accretion-related metamorphism of the Metchosin Igneous Complex, southern Vancouver Island, British Columbia, *Can. J. Earth Sci.*, *42*(8), 1467–1479.
Tucholke, B. E., J. Lin, and M. C. Kleinrock (1998), Megamullions and mullion structure defining oceanic metamorphic core complexes on the mid-Atlantic ridge, *J. Geophys. Res.*, *103*(B5), 9857–9866.
Turcotte, D. L., and G. Schubert (2002), *Geodynamics*, 2nd ed., Cambridge Univ. Press, N. Y.
Vogt, K., and T. Gerya (2014), Deep plate serpentinization triggers skinning of subducting slabs, *Geology*, *42*(8), 723–726.

Wada, I., and K. L. Wang (2009), Common depth of slab-mantle decoupling: Reconciling diversity and uniformity of subduction zones, *Geochem. Geophys. Geosyst.*, *10*, Q10009, doi:10.1029/2009GC002570.

Wells, R. E., D. C. Engebretson, P. D. Snavely, and R. S. Coe (1984), Cenozoic plate motions and the volcano tectonic evolution of Western Oregon and Washington, *Tectonics*, *3*(2), 275–294.

Yamato, P., P. Agard, E. Burov, L. Le Pourhiet, L. Jolivet, and C. Tiberi (2007), Burial and exhumation in a subduction wedge: Mutual constraints from thermomechanical modeling and natural P-T-t data (Schistes Lustres, western Alps), *J. Geophys. Res.*, *112*, B07410, doi:10.1029/2006JB004441.

Yamato, P., E. Burov, P. Agard, L. Le Pourhiet, and L. Jolivet (2008), HP-UHP exhumation during slow continental subduction: Self-consistent thermodynamically and thermomechanically coupled model with application to the Western Alps, *Earth Planet. Sci. Lett.*, *271*(1–4), 63–74.